von Karman Institute for Fluid Dynamics

Lecture Series 1991-08

Laser Velocimetry

June 10 - 14, 1991

Generation of Particles and Seeding

James F. Meyers
NASA - Langley Research Center
Hampton, Virginia, USA

Generation of Particles and Seeding

by

James F. Meyers
NASA - Langley Research Center
Hampton, Virginia 23681
United States

Introduction

One of the most important elements in laser velocimetry, yet the most neglected, is the small particle embedded in the flow field that scatters the light necessary to make velocity measurements. The characteristics of this lowly particle are often ignored in the effort to obtain data. This seems strange since it is the primary cause of measurement error. If the particle is too large, it will not follow the flow resulting in an inaccurate representation of the fluid velocity. If the particle is too small, it will not scatter sufficient light to provide the signal-to-noise necessary to minimize measurement uncertainty in the signal processing electronics.

When the researcher finally gets around to deciding on the material to be used for the seed particles and the method for their generation, he is faced with a myriad of possibilities. Asking the advice of others leads to frustration since, like politics and religion, everyone has their own belief in the best method—*And don't confuse them with facts stating otherwise*.

This lecture will attempt to remove the confusion in choosing a seeding method by assessing many of the techniques currently used. It will outline their characteristics and typical limitations imposed by various applications. The lecture will then focus on the ramifications of these methods on measurement accuracy.

The Effect of Particle Size on Laser Velocimetry

Choosing the proper seeding particle for laser velocimetry applications is a classic case of compromise. A smaller particle will more faithfully follow the fluid flow increasing measurement accuracy, while a larger particle will scatter more light increasing signal strength resulting in greater measurement precision. The chosen particle size is often determined by the ability of the optical system to *see* that particle and aerodynamic inaccuracies accepted. The sensitivity of the optical

system is in turn constrainted by facility, optical, and financial limitations. While this lecture will not attempt to establish specifics, it will provide examples that illustrate the trade-offs that may serve as guidelines in choosing the best compromise.

Light Scattering

From classical electromagnetic theory, the scattering process is a function of particle size, wavelength of the impinging light, and the optical characteristics of the scattering material. For particle sizes on the order of the wavelength, the appropriate theory is given by Mie, reference 1. The scattering cross section, σ_{Mie}, describes the complex electromagnetic field scattered from a spherical particle with index of refraction n from an impinging plane wave:

$$\sigma_{Mie} = \frac{i_{\perp}(\alpha_1, n, \theta) + i_{\parallel}(\alpha_1, n, \theta)}{2k^2} \tag{1}$$

where

$i_{\perp}(\alpha_1, n, \theta)$, $i_{\parallel}(\alpha_1, n, \theta)$ — intensity of light with electric vector perpendicular and parallel, respectively, to the plane through the direction of propagation of the incident light and viewed scattered light. These intensities are solved as Taylor series expansions using a computer code developed by McCormick, reference 2.

α_1 — particle size parameter, $\frac{2\pi r}{\lambda}$

n — index of refraction

θ — angle between incident light and viewed scattered light

k — wave number of incident radiation, $\frac{2\pi}{\lambda}$, meter^{-1}

The characteristics of Mie scattering can be illustrated by choosing a laser wavelength, e.g., 514.5 nm, and several particle sizes with a given index of refraction, e.g., 1.5 + i0.0. The component electric vectors are shown in figure 1 for 0.2, 0.4, 1.0, and 4.0 micron diameter particles as a function of scattering angle. The complex nature and large dynamic range of Mie scattering is easily seen. The general assumption that a larger particle will scatter more light greatly depends on the viewing

angle. For example, at 40-degrees backscatter, a 1.0 micron particle scatters more light than a 4.0 micron particle. The change in Mie scattering as a function of particle size is illustrated in figure 2 for the same index of refraction at a viewing angle of 2-degrees forward scatter. The scattered light drops very quickly below 0.8 micron whereas it plateaus above.

These Mie scattering cross sections can be used to determine the signal characteristics obtained from laser transit anemometers, particle image velocimetry, and Doppler global velocimetry. However, reference beam and fringe type laser velocimeters use light from two sources. The interaction of the plane wave reference beam with collected scattered light requires an alignment of the two light waves to a quarter wave tolerance to avoid interference effects on the photocathode surface that suppress heterodyning. Particles passing through the measurement volume of the fringe type laser velocimeter simultaneously scatter light from both focused laser beams. Since the two scattered waves are coherent they will interfere on the photocathode surface based on the relative phases of the two Mie scattering cross sections. Adrian and Earley developed procedures to describe the complex Mie scattering cross section for two input light waves in reference 3.

Particle Dynamics

Since the laser velocimeter measures the velocity of small particles embedded in the flow and not the flow itself, measurement accuracy directly depends on the ability of these particles to faithfully follow the fluid flow. The motion of a particle in a fluid was studied by Oseen, reference 4, who derived the equation of motion for a spherical particle in a fluid at rest. Tchen, reference 5, extended the equation to determine the motion of a particle in a fluid moving with a variable velocity. The incorporation of the drag coefficient, C_D, by Soo, reference 6, yields the following relation:

$$\frac{\pi}{6} D_p^3 \rho_p \frac{dV_p}{dt} = \begin{cases} \frac{\pi}{6} D_p^3 \rho_p \Lambda (V_g - V_p) \\ -\frac{\pi}{12} D_p^3 \frac{dP}{dD_p} \\ +\frac{\pi}{12} D_p^3 \rho_g \frac{d}{dt}(V_g - V_p) \\ +\frac{3}{2} D_p^2 \sqrt{\pi \rho_g \mu} \int_{t_0}^{t} d\tau \frac{\frac{d}{d\tau}(V_g - V_p)}{\sqrt{t-\tau}} \end{cases} \qquad (2)$$

where

$$\Lambda = \frac{3}{4} C_D \frac{\rho_g}{\rho_p D_p} |V_g - V_p|$$

D_p	diameter of the particle
ρ_p	density of the particle
$\frac{dV_p}{dt}$	acceleration of the particle
ρ_g	density of the fluid
V_g	velocity of the fluid
V_p	velocity of the particle
P	pressure of the fluid
μ	viscosity of the fluid
t	time

Each term in equation (2) is a force that affects the motion of the particle in the flow. The term on the left side of the equation is the total force required to accelerate the particle in the fluid. This force is comprised of the viscous resistance to motion, i.e., Stoke's drag; the force from the pressure gradients in the fluid surrounding the particle; the force required to accelerate the apparent mass of the particle relative to the fluid; and the Basset term that takes into account deviations from steady state. Soo, reference 6, and Hinze, reference 7, state that when the particle density is much greater than the fluid density, the Stoke's drag is the dominant term on the right-hand side of equation (2). Since the seeding particles satisfy this requirement in gas flows, equation (2) reduces to:

$$\frac{\pi}{6} D_p^3 \rho_p \frac{dV_p}{dt} = \frac{\pi}{6} D_p^3 \rho_p \Lambda (V_g - V_p) \tag{3}$$

The effective Reynolds number between the gas and the particle may be defined as follows:

$$\mathrm{Re} = \frac{\rho_g |V_g - V_p| D_p}{\mu} \tag{4}$$

Substituting Λ and Re into equation (3), the particle acceleration relation is found:

$$\frac{dV_p}{dt} = \frac{3}{4} \frac{C_D \, \mu \, \mathrm{Re}}{\rho_p \, D_p^2} (V_g - V_p) \tag{5}$$

Meyers and Walsh, reference 8, refined the drag coefficient by incorporating corrections to match empirical data where the relative Mach number, M_p, is less than 0.5:

$$C_D = \frac{\overline{C}_D + \frac{51.1}{\mathrm{Re}} M_p}{1.0 + 0.256 \; M_p (\overline{C}_D + \frac{51.1}{\mathrm{Re}} M_p)} \tag{6}$$

where

$$\overline{C}_D = \frac{24}{\mathrm{Re}} + 0.4 + 1.6 \, e^{-0.028 \, \mathrm{Re}^{0.82}}$$

$$M_p = \frac{|V_g - V_p|}{\sqrt{K_{sp} \, RT}}$$

K_{sp} ratio of specific heats

R specific gas constant

T temperature

The motion of a particle described by these equations can be illustrated by following the particle as it passes through an oblique shock, figure 3. The flow velocity instantly decreases from 1350 ft/sec to 1175 ft/sec at the shock but the particles take longer to respond. For example a 1 micron particle takes 0.25 inches to reach the proper velocity whereas it takes a 5 micron particle over 4 inches. Therefore the accuracy of laser velocimeter measurements downstream of the shock will depend on the size of the seeding particle and the location of the measurement volume.

The time history of a particle injected into a low speed fluctuating flow, figure 4, not only shows a delay for the particle to reach the flow velocity, but shows a continued phase lag behind the velocity fluctuations. Although the phase lag is normally unimportant, the decreased amplitude of the velocity fluctuations by the particle constitute a

measurement error. Unfortunately the magnitude of this error is difficult to determine because the frequency of the forcing function may not be known nor measurable. For example, if a uniform succession of eddies, shown in figure 5, convect past a hot wire at some mean velocity, the wire records, in this case, 12 changes in velocity per unit time. If the mean velocity is halved, the number of changes per unit time is also halved though the eddies remain the same. Particles present in the flow, illustrated in the bottom figure, only need to respond to the changes in velocity directed on it by the growth and decay of the eddies and not as measured by a stationary probe. The required frequency response of the particle is much less than the fluctuating frequencies measured by a hot wire, but how much less is unknown.

The transformation of particle lag from the theoretical world to the real world can be illustrated by measuring the velocity of particles along the stagnating streamline of a hemisphere-cylinder, reference 9. This investigation was conducted in the Langley 16-foot transonic tunnel. The particles were obtained by atomizing 10 weight motor oil using an air/oil atomizer located on the final set of turning vanes prior to the test section. The resulting measurements along with the theoretical gas velocity are presented in figure 6 for various Mach numbers. While the distance from injection to the test section is sufficient to bring the particles up to free stream, they do not respond to the stagnating flow field at all. Using equation (5) to predict the velocity history along the stagnating streamline for various particle sizes, figure 7, it can be seen that the injected particles were greater than 25 microns in diameter. Clearly useful laser velocimetry data cannot be obtained using atomized 10 weight motor oil. Before continuing with further testing of this flow field, let us review several commonly used particle generators.

Candidate Particle Generating Systems

At this point let us delve into the world of religion and politics by reviewing several methods to solve the particle generation problem. These *solutions* include atomizers of various types, vaporizers, injectors, and fluidized beds. Let us begin with our ex-favorite—the atomizer used in the stagnating streamline investigation.

The oil/air atomizer, shown in figure 8, is a sophisticated perfume sprayer. Air is forced through a small jet which blows over a reservoir of oil. The combination of capillary effect and reduced pressure within the jet causes the oil to rise within the oil gap where the jet shears it into small particles. The size of each particle will depend on how much liquid is sheared to form that particle, the surface tension of the liquid, and the amount of evaporation prior to reaching the measurement volume.

Clearly this type of generator lacks sufficient control of particle size to be a candidate system based on the stagnating streamline test.

A variation of the oil/air atomizer is the laskin nozzle, shown in figure 9. The major difference is the immersion of the atomizer within the liquid. The generated particles are contained within bubbles produced by the air jet. These particles are released when the bubbles reach the surface. This method reduces the number of large particles since they will not remain suspended within the bubbles. Using di-octyl phthalate with a laskin nozzle, Yanta, reference 10, produced particles smaller than 2 microns. Yanta also placed an impactor on the generator output to further reduce the particle size, figure 10, for application in supersonic wind tunnels.

Other variations of the basic atomizer include systems which force liquid through a small orifice breaking the liquid into small particles. The liquid could be forced with pressurization or by using injectors. These systems produce sufficient particles, but the sizes are usually large. The addition of a piezoelectric crystal to vibrate the orifice reduces the particle size and, under careful adjustment, results in near monodisperse operation.

Another classification of particle generator is the vaporization/ condensation generator illustrated in figure 11. This generator heats an oil/air mixture to produce a hot vapor which condenses as it cools when leaving the generator. Changing the output orifice to vary the output velocity and thus the rate of cooling, a crude control of particle size is obtained. An example of this control is illustrated in figure 12 using Dow Corning 704 diffusion pump oil. The resulting particle size distribution is similar to that obtained with a laskin nozzle except the particle generation rate is upwards of two orders of magnitude greater. Simpler versions of a vaporization/condensation generator used to provide theatrical smoke drip propylene glycol onto a hot plate. Propylene glycol is nontoxic and evaporates completely within a few minutes after particle generation. However, evaporation can have an effect on particle size and number density as shown in figures 13 and 14 making this generator unreliable for consistent operation.

These generators all have one common trait—the use of a liquid as the seed material. Liquids cannot be used at high temperatures because of evaporation or at worse flammability. Pressure changes cause the surface tension to vary, thus changing the resulting particle size distribution. Applications in these environments require the use of solid particles, typically aluminum oxide, titanium oxide, silicon carbonate or aluminum silicate. The particles are typically injected using a fluidized bed to aerate and separate the particles and provide an

air medium to carry the particles to the flow. Let us return to the stagnating streamline test again, this time armed with aluminum silicate, figure 15.

In Situ Characteristics of Aluminum Silicate in the 16-foot Transonic Tunnel

The previous investigations in the 16-foot transonic tunnel using 10 weight motor oil and kerosene, reference 11, indicated that the liquid particles were too large. The particle size may have been controlled more by conditions within the tunnel, 0.5 atmosphere pressure and 90°F above ambient, than the generator or the fluid. Solid particles composed of hydrous aluminum silicate were used in a detailed investigation to develop a seeding system for the 16-foot transonic tunnel that would provide particles sufficiently small to increase measurement accuracy, reference 12.

The investigation began by measuring the particle size distribution in the laboratory using an aerodynamic particle size analyzer. The aluminum silicate particles were suspended in ethanol that was then atomized using a standard oil/air atomizer. The ethanol droplets evaporated quickly leaving the aluminum silicate particles to follow the flow field. The particles are irregular in shape with a specific gravity of 2.58 and an index of refraction of 1.56. The aerodynamic particle size analyzer equates the size distribution of the aluminum silicate to the diameter of equivalent spherical particles. The particle size distribution presented in figure 16(a) shows a long trailing distribution function toward larger particle sizes. This trailing distribution may be the result of large particles, agglomeration of smaller particles, or possibly alignment of the irregularly shaped particles with the flow in different orientations. Since the particle size analyzer determines the particle size by measuring the aerodynamic particle response to a known acceleration flow field, the same behavior should be expected within the tunnel flow.

The ability of the laser velocimeter to measure these particles was determined by modeling the optical system with the computer simulation given in reference 8 with updates using the Mie scattering theory presented by Adrian and Earley in reference 3. The system focal length was chosen to be 3 m to place the measurement volume on the tunnel centerline. The particle velocity was chosen to be 420 m/sec. The laser velocimeter sensitivity factor (probability of making a measurement) was formulated by first determining whether a particle of given size passing through the center of the sample volume would yield a velocity measurement. If so, then it was determined how far

away from the center the particle could pass and still yield a measurement. This was done in the following manner.

The calculation of the measurement probability begins with determination of the electromagnetic field resulting from the scatter of light from a particle of a given size, reference 1, as it passes through each of the pair of laser beams comprising the measurement volume. The interaction between the two scattered fields is calculated over the collecting solid angle of the laser velocimeter using the method described by Adrian and Earley in reference 3 to yield the optical transfer function. This function is used with the Gaussian intensity profile of the laser beams to obtain the theoretical signal burst. The burst is integrated and used to drive a Poisson random number generator to yield a Monte Carlo simulation of photon arrivals at the photocathode surface of the photomultiplier. The statistically determined photo-electron pulse train is convolved with the photomultiplier transfer function to obtain the electronic signal burst. The burst is then input to a model of a high-speed burst counter with double threshold detection circuits and 5:8 count comparison to determine whether the signal has sufficient amplitude to yield a velocity measurement. If the signal, following band-pass filtering, does not have sufficient amplitude for 10 consecutive cycles to cross the thresholds with sufficient signal-to-noise ratio to satisfy the 5:8 comparison test, a measurement cannot be made and the sensitivity factor is zero for that particle size. If the signal is accepted by the counter, the amplitude of the signal is reduced exponentially until the signal fails to be accepted by the counter. The amount of reduction in amplitude corresponds to a distance from the center of the measurement volume according to the Gaussian intensity profile of the laser beams. A sensitivity factor of unity is arbitrarily assigned when the distance from the center of the measurement volume corresponds to the measurement volume radius, defined by the intensity being $1/e^2$ of the intensity at the center. The resulting sensitivity factors corresponding to the appropriate particle sizes measurable by the aerodynamic particle size analyzer are presented in figure 16(b). Multiplying the particle size distribution, figure 16(a), by the corresponding sensitivity factor profile, figure 16(b) yields the detectable particle size distribution, figure 16(c). The mean size of the measured aluminum silicate particles was found to be 0.5 microns with a standard deviation of 0.17 microns. From the simulation, the mean detectable size of particles that will yield velocity measurements is 0.78 microns with a standard deviation of 0.28 microns.

The theoretical particle velocity history along the stagnating streamline of the hemisphere-cylinder model was determined using the program presented in reference 8. The resulting particle velocities were

predicted to deviate as much as 2.73 m/sec from the expected gas velocity, at x/D = -0.133 (the point of maximum deceleration) at Mach 0.8 for particles as small as 1 micron in diameter. Particle velocities were then measured from one model diameter upstream, where the mean velocity is nominally 11.5 percent below free-stream conditions due to the presence of the model, to within an estimated distance of 1.9 mm from the model surface for tunnel settings of Mach 0.8 and Mach 1.0. In addition, the velocity flow field was measured at Mach 1.0 at y/D = -0.533 since the moderately decelerating flow along this line changes to an accelerating flow as the model is approached until the shock line is reached.

The detailed analysis of the data begins by considering the known test information. From the particle size analysis given previously for the aluminum silicate particles and the predicted sensitivity of the laser velocimeter, the average detectable particle diameter was estimated to be 0.78 microns. The predicted velocity profiles for the three test cases were determined according to the procedure outlined in reference 13 using the tunnel calibration to establish the free-stream conditions. The potential flow method outlined in reference 13 does not include viscous effects, for example, shock wave and boundary layer effects, which are potentially significant at the transonic Mach numbers of 0.8 and 1.0. It is estimated from prior experience that this computational method yields predictions with accuracies roughly ±2 percent. The resulting predictions of the gas flow characteristics were used with the particle dynamic prediction procedures from reference 14 to determine the velocities of the average detectable particle, which provide the theoretical reference for comparison with the velocity measurements from the laser velocimeter. The second area of information is that errors in the measurement of cross beam angle yield an unknown bias in the laser velocimeter measurements. The cross beam angle was measured geometrically at a distance of 2.5 m from the measurement volume with an estimated uncertainty of ±1 mm in determining the center of the 13.1-mm-diameter laser beams. This uncertainty yields an unknown bias error in the measurement of the mean velocity within the range of ±1.45 percent. The final known information is that the model moved downstream during the test because of sting bending, compression of the sting drive gears, etc. This was determined by visually establishing a reference point with the sample volume at the center surface pressure port on the model during setup and finding that the flare that occurs when the sample volume grazes the model was not detected during the test until the laser velocimeter was moved 0.63 mm downstream of the reference point. This distance is not an exact measure of the deflection since flare is detected when the edge of the sample volume (not necessarily the $1/e^2$ intensity location) grazes the model; however it does indicate a movement of the model. The reference

point was checked (again visually) following the test and found to repeat the reference point.

It was found that the particle trajectory that best fits the measurement data, figures 17 - 19, is based on an aluminum silicate particle with a diameter of 2.1 microns, whereas the average detectable particle diameter predicted from the aerodynamic particle size analyzer and the laser velocimeter simulation code is 0.78 microns. In an attempt to understand the discrepancy, the sensitivity threshold in the laser velocimeter simulation was raised, since the laser velocimeter characteristics were determined following optimization of the system in the laboratory after the wind tunnel tests were completed and are known not to represent the degraded conditions of the system while in the wind tunnel (gradual misalignment due to tunnel vibrations causing a loss in optical system efficiency). This attempt was able to raise the average detectable particle diameter to only 1.4 microns. The effect of the irregularly shaped particles in an optical sense was then determined by measuring the particle size distribution with an optical particle size analyzer, figure 20. This resulted in a different size distribution from that obtained with the aerodynamic analyzer, figure 16, which results in a different detectable particle size distribution when multiplied by the laser velocimeter sensitivity function. The calculation of the mean detectable particle size based on the new distribution function yields a particle diameter of 2.33 microns. This shows that a particle of a single aerodynamic size scatters light at different levels depending on the orientation of the irregularly shaped particle as it passes through the optical size analyzer and likewise through the laser velocimeter measurement volume. Therefore the predicted laser velocimeter sensitivity function, which is calculated based on the assumption of spherical particles, can be used to provide only a rough approximation in this test situation.

As an aid in understanding the aerodynamic process involved in the present situation, consider the effect on the laser velocimeter measurements of the polydisperse particle distribution within the decelerating flow field as a combination of effects from each particle size. If the probability density function of the gas velocity at a location in the decelerating region is represented by figure 21(a), a uniform polydisperse particle size distribution (e.g., seven particle sizes) within the flow would result in the probability density function given in figure 21(b). By considering the polydisperse particle size distribution as being made up of individual particles, one finds that a zero-diameter particle would result in the translation of the velocity distribution figure 21(a) to the left or lowest velocity side of the distribution in figure 21(b). As the particle size increases, the velocity distribution is shifted to the right (higher velocity) because of the lag in the response of

the particle to the decelerating flow field. Therefore the resulting probability density function of particle velocity would be determined by a convolution of the probability density function of the gas velocity with the particle velocity lag characteristics as a function of particle size at that point in the flow field. Figure 21(b) shows that for a uniform distribution of particle sizes the center of the velocity probability density function is approximately flat; thus, variations in the center of the density function yield an estimate of the particle size distribution in the flow. Therefore the measured velocity histograms in the decelerating region along the stagnating streamline may be used to estimate the particle size distribution detected by the laser velocimeter within the flow. From this distribution coupled with the particle size distribution measured by the aerodynamic particle size analyzer, the sensitivity function can be estimated. The measured velocity histograms were compared with the velocity trajectories for the particle sizes measured by the aerodynamic analyzer using the histogram divisions from the optical particle size analyzer, figure 22. It was found that at x/D of -0.5 and -0.4, there was sufficient spread in velocity due to particle size while the measured local *turbulence intensity* remained low (approximately 2 percent). Assuming that velocities within the histogram below the predicted gas velocity were due to turbulence and removing them along with the corresponding high velocities, the remaining velocity distribution should be due to particle lag differences. Each velocity in the truncated histogram was equated to the particle size required to yield that velocity as predicted by the theoretical particle velocity profiles, figure 23(c). The particle size histogram measured by the aerodynamic analyzer, figure 23(a), was then divided into the truncated histogram to yield the sensitivity function. It may be seen from figure 23(b) that the resulting sensitivity function resembles the theoretical sensitivity function in figure 22(b) with the differences found at the extremes, most likely from statistical uncertainties due to the low particle count at the corresponding velocities thus distorting the sensitivity function. The average detectable particle size determined from the truncated histogram was 2.17 microns in diameter with a standard deviation of 0.76 microns.

Solids at High Speed

Now that we seem to be heading in the right direction, let us push our luck and go supersonic. As in the 16-foot transonic tunnel test, a theoretically predictable flow field was chosen to establish the performance of the particle seeding method. As shown in figure 3, an oblique shock is a simple flow that can used to measure the particle size. Since Mach 1.3 is not very fast, the test was conducted in the Langley 20-inch Mach 6 wind tunnel, reference 15. A flat plate was placed in the

tunnel at an inclined angle, δ, of 30 degrees, figure 24, resulting in an oblique shock at an inclined angle, θ, of 40.8 degrees. The tunnel conditions were set to 3.28×10^6 N/m^2 (475 psi) total pressure and 520° K (935° R) total temperature.

A fluidized bed, figure 25, was used to deliver 0.3 micron aluminum oxide particles to the tunnel settling chamber. The bed is designed to withstand 6.9×10^6 N/m^2 (1000 psi) and contain sufficient seed material for several tunnel runs. The bed was aerated by forcing air through a porous brass plug at the bottom of the chamber using a differential pressure of 690 N/m^2 (0.1 psid).

The measured velocity history behind the shock is shown in figure 26 along with predicted histories for 0.8, 1.0, and 1.2 micron aluminum oxide particles. Based on these results, the 0.3 micron aluminum oxide agglomerated yielding an effective particle diameter of approximately 1.1 microns in the tunnel. After several test runs, the supply of aluminum oxide was exhausted. A factory fresh supply was opened and the fluidized bed filled. The next two runs resulted in a smaller particle size, 0.6 microns, figure 27. These results show that aluminum oxide agglomerates, but less so when kept dry. Opened containers will absorb water vapor increasing the amount of agglomeration.

Where Do We Go From Here

In summary, several particle seeding techniques for laser velocimetry applications have been presented. These techniques include atomizers and vaporization/condensation generators using liquids, and fluidized beds and liquid carriers for solid particles. All of these techniques have a major flaw, they generate polydisperse particle distributions. The test results in the 16-foot transonic tunnel clearly show the effects of these distributions on laser velocimeter measurements. Unknown bias errors in the mean velocity due to particle lag and artificial increases in measurement standard deviation may result in unacceptable measurements. If known monodisperse particles could be used, these problems would be avoided. Further, signal-to-noise would be increased since most noise present in the photomultiplier output is due to small particles scattering insufficient light to yield a measurable signal.

In fact, monodisperse spherical polymeric particles in the desired diameters are commercially available and were used on a limited basis with excellent results in some small wind tunnel tests at Langley. However, the cost is prohibitive for large wind tunnel applications due to the quantity of particles required and hence have not been used. Since the potential benefits of using these particles are so great,

Nichols, reference 16, began an investigation to determine the feasibility of producing polymeric particles at Langley. Initial experiments were directed toward emulsion polymerization using surfactants, references 17 and 18, but it was quickly learned experimentally that mondispersity was difficult to achieve by this method. Emulsifier-free polymerization, reference 19, was then tried with excellent results. Emulsifier-free polymerization can be carried out only at a relatively low concentration of solids, i.e., approximately 10 volume percent in water. The section following is a description of the technique to make low cost, monodisperse polystyrene particles from 0.6 to 2.7 microns.

The Making of Monodisperse Polystyrene Particles

The clearest way to describe the process to make monodisperse polystyrene particles is in cookbook form. The apparatus is first described followed by the procedure. High power microscope photographs of the resulting particles are then shown to demonstrate their uniform size. This technique has been successfully used by several research laboratories to construct their own particles. If you attempt to make these particles, be patient—there is an art to it. Iterate the procedures as chemical purity can vary yielding varying results. With experience, they become very simple to make.

Apparatus for Making Polystyrene Particles

The apparatus, shown in figure 28, consists of a 3-liter Pyrex reaction kettle having temperature controlled by a heating mantle and a cold finger condenser circulating tap water. This control is operated by a mercury thermoregulator that alternately calls for heating or cooling depending on the set temperature versus the sensed temperature. A condenser returns any vaporized reactants to the reaction vessel. A gas inlet adapter atop the condenser allows a nitrogen purge. A *home-made* stirring paddle, shown full-scale in figure 29, insures sufficient agitation of the reactants. Shaft size is not important and can be sized to use whatever bushing is at hand.

Following is a list of catalog numbers for various components of the apparatus, keyed to figure 28:

(1) No. 6947, Pyrex Kettle w/4 neck cover, 3000 ml (Corning Glass Works)

(2) Condenser, cold finger (Ace Glass Inc., No. 5950)

(3) Mercury Thermoregulator (Precision Scientific, No. 62539)

(4) Condenser (Ace Glass Inc., No. 5945)

(5) Adapter, Gas Inlet (SGA Scientific, Inc., No. JA 7970)

(6) Stainless Steel Stirring Paddle (figure 29)

(7) Armoured Heating Mantle, 4 Liter (Glass-Col, Catalog No. TM 580)

Equivalent components from other manufacturers are also acceptable. The manufacturer is mentioned here only to present an accurate record as to what was actually done during experimentation.

The Procedure for Making Polystyrene Particles

1. Select formulation from Table 1 for the desired particle size.

2. Charge the reactor in the following order: water, magnesium sulfate electrolyte solution (if required), and styrene.

3. Bubble nitrogen gas through the above mixture for 40 minutes in order to purge all oxygen from the reactor (approximately 0.5 liters/min flow rate) using a gas dispersion tube (Pyrex, ASTM 170-220 or equivalent). Remove tube from the reactor after 40 minutes and place nitrogen line onto the gas inlet adapter atop condenser, maintaining this nitrogen purge throughout the entire run.

4. Start agitator (150 rpm) and begin heating to 65° C.

5. When the temperature stabilizes at 65° C, as evidenced by several cycles of the temperature controller, add potassium persulfate solution to the reactor via pipet insuring that the pipet tip is several inches below the liquid surface. This places the initiator well beneath the styrene layer on top and into the reaction zone in the water layer where the polymerization takes place. Run for 24 hours (beginning with the addition of the potassium persulfate).

6. After the 24 hour period unplug the temperature controller and stop agitation. After cooling for a few minutes, remove any sticky, rubbery material that may form a separate layer on the top with paper towels. Filter through 100 mesh cheese cloth into a clean

storage container. Filtration removes any coagulum or sticky substance from the particles. Please note that some styrene may polymerize on the stirring blade. The polystyrene adheres to the blade but can be removed by soaking in xylene overnight.

7. (Optional) If particles are to be stored longer than several months, it is advisable to place the sealed container of particles into a 65-70° C oven for 24 hours. This will minimize any chance for biological growth as the particles appear to be an ideal culture medium. If you use this step, sample for weight percent solids after step 6.

Sample for Weight Percent Solids

Pipet approximately two to four ml of particles each into two small pre-weighted disposable aluminum sampling pans. Weigh the respective samples and place in a 65-70° C oven for several hours until dry. Reweigh each pan and calculate the weight percent solids by using the following formula:

$$w/o = \frac{100\,(w_f - w_t)}{(w_i - w_t)} \qquad (7)$$

where w/o weight percent

w_f weight after drying

w_i weight before drying

w_t tare weight

The w/o solids should be approximately 7.3 percent.

Assessing the Results

A Nikon Microphot -FX Microscope at 2000X was used to determine particle size. This was done with Polaroid Photography by comparing an NBS 474 AR Chromium Photomask Optical Linewidth Standard, reference 20, at 2000X with a photograph of the particles at the same magnification. One drop of the undiluted particles was placed on a microscope slide and smeared by slowly scraping with a cover slide held on one edge. After drying in a dessicator (about one hour) the slide was then photographed under the microscope. A properly prepared slide will have regular arrays of particles as shown in figure 30. Measurements

should be made from center to center of the longest straight array of particles possible being very careful to avoid any arrays that exhibit microcracks. If microcracks are not avoided, erroneous measurements will be obtained. Since some microcracks are extremely difficult to discern, it is best to make as many measurements of different arrays as possible and then average the results. Obviously any measurements that are suspected of containing microcracks should be eliminated from the average. Results using this method have been found to agree with Scanning Electron Microscope measurements to within 0.1 micron.

Formulating the Chemical Solutions

Magnesium Sulfate and Potassium Persulfate solutions were made using deionized water of 16-18 megohm-centimeter purity. The 1 *w/o* solution is made by weighing out 10.0 grams of the respective chemical into a 1-liter volumetric flask and filling to the 1-liter mark with deionized water. Use of less pure water may result in a somewhat different particle size but should not affect monodispersity. In a similar manner, the 3 *w/o* solution is made by using 30.0 grams of the chemical rather than 10.0 grams, all other factors being the same. Note that in Table 1, some formulations use 3 *w/o* potassium persulfate in lieu of 1 *w/o*. Actually one should work as well as the other with proper adjustment of volumetric quantity but the 3 *w/o* is used due to an inadequacy in the setup. Step 4 in the procedure calls for heating to 65° C. As this step occurs before addition of potassium persulfate, the total volume is such that the thermoregulator bulb does not touch the liquid and hence temperature control is not possible. By using 3 w/o potassium persulfate, the initial volume is large enough to allow submersion of the thermo-regulator bulb. A slightly different setup would allow the thermo-regulator bulb to contact the liquid in which case 1 w/o could be used for all formulations.

For reasons not fully understood at present, small variations in particle size from the values given in Table 1 do occasionally occur, but these variations do not affect monodispersity. Increasing the amount of magnesium sulfate tends to give larger particles while a decrease results in somewhat smaller particles.

All chemicals used were obtained from Polysciences:

Magnesium Sulfate, ultra pure, Catalog No. 1623
($MgSO_4 \cdot 7H_2O$)

Potassium Persulfate, Catalog No. 1057

Styrene, Catalog No. 0660

Equivalent grades from other sources are obviously also acceptable. The supplier is mentioned here only to present an accurate record as to what was actually done during experimentation.

Table 1.- Formulations for Polystyrene Latex, Monodisperse, Spherical

	Particle Diameter, microns				
	0.6	1.0	1.7	2.0	2.7
Water, ml	2489	2329	2369	2200	2339
Magnesium Sulfate, ml	0	56	56	56	56
Concentration, *w/o*	1	1	1	1	1
Styrene, ml	265	265	265	265	265
Potassium Persulfate, ml	46	150	110	278	139
Concentration, *w/o*	3	3	3	1	1

Using Polystyrene Particles for Laser Velocimeter Applications

Now that the low cost, monodisperse polystyrene particles have been made, the next task is to inject them into the flow field. Since the particles are suspended in water following their manufacturer, injection with normal atomizers is the simplest method. They need to be further deluted to keep the atomizer from clogging and to reduce the data rate to desired levels. The deluting liquid should be a 50-50 solution of water-ethanol. This solution evaporates very quickly leaving the particles behind to follow the flow. Pure water nor pure ethanol evaporate as quickly and form larger droplets upon exiting the atomizer. Large droplets may contain more than one polystyrene particle that will yield an agglomerated particle when the liquid evaporates. Monitoring oscilloscope traces from the laser velocimeter provide evidence that the signal-to-noise is greatly improved over other materials and that only single, nonagglomerated particles occur.

Polystyrene particles are now used in all laser velocimetry applications at Langley with the exception of supersonic wind tunnels and combustion experiments where aluminum oxide is used as polystyrene would not survive the high temperatures. Even seeding large tunnels such as the 4x7- meter low speed wind tunnel become practical when the particles cost less than a dollar per liter versus over $3000 per liter for commercial particles. The seeding system for this tunnel, shown in figure 31, holds an array of 20 agriculture spray nozzles to deliver the

liquid suspended particles. The array location can be remotely controlled to place the particle plume anywhere in the test section. While this huge system, covering a 15x15- meter settling chamber, was expensive, it has doubled measurement productivity in the wind tunnel.

Summary

The major categories of particle generation techniques for laser velocimeter applications have been presented. Techniques using liquids yield polydisperse particle size distributions that may vary in mean and standard deviation depending on the material, the generating technique, and the external environment. These techniques produce many small particles that do not scatter sufficient light to be measured, but add to the background light level decreasing the signal-to-noise of particles that can be measured. As illustrated in a companion lecture, low signal-to-noise will result in increased measurement standard deviation and a corresponding increase in statistical uncertainty in the mean velocity. Therefore liquid seeding particles should be avoided. Solid particles such as aluminum oxide, aluminum silicate, titanium oxide, silicon carbonate, etc. are also polydisperse but typically narrower than liquid distributions. The particle size may increase because of particle agglomeration as shown in the Mach 6 experiments. These solids should only be used in high temperature environments where care is taken to insure a minimum agglomeration. The best seeding particles are polystyrene because they are spherical, light (specific gravity of 1.05) with a high index of refraction (1.59 + i0.0), monodisperse and, when injected with water-ethanol, do not agglomerate.

Acknowledgment

I wish to thank Mr. Cecil Nichols for his work in the development of polystyrene paticles for laser velocimetry applications. His efforts have greatly increased the quality and quantity of laser velocimeter measurements at NASA - Langley Research Center. His willingness to share his experience, including the description of his process for making the particles in this lecture, has increased the value of the technique to fluid mechanics research.

References

1. Mie, G.: *Optics of Turbid Media.* Ann. Phys., vol. 25, no. 3, 1908, pp. 377-445.

2. McCormick, M.P.: *Laser Backscatter Measurements of the Lower Atmosphere*. Ph. D. Thesis, College of William and Mary in Virginia, 1967.

3. Adrian, R.J.; and Earley, W.L.: *Evaluation of LDV Performance Using Mie Scattering Theory*. Proceedings from the Symposium on Laser Anemometry, University of Minnesota, January 1976, pp. 426-454.

4. Oseen, C.W.: **Hydrodynamik**. p. 132, Leipzig, 1927.

5. Tchen, C.M.: *Mean Value and Correlation Problems Connected with the Motion of Small Particles Suspended in a Turbulent Fluid*. Ph. D. Thesis, Delft, 1947.

6. Soo, S.L.: **Fluid Dynamics of Multiphase Systems**. Blaisdell Publishing Co., 1967.

7. Hinze, J.O.: **Turbulence**. McGraw-Hill Book Co., 1959.

8. Meyers, J.F.; and Walsh, M.J.: *Computer Simulation of a Fringe Type Laser Velocimeter*. Proceedings of the Project Squid Workshop on the Use of the Laser Velocimeter for Flow Measurements, Purdue University, March 27-29, 1974, pp. 471-509.

9. Meyers, J.F.; Couch, L.M.; Feller, W.V.; and Walsh, M.J.: *Laser Velocimeter Measurements in a Large Transonic Wind Tunnel*. Proceedings of the Minnesota Symposium on Laser Anemometry, University of Minnesota, October 22-24, 1975, pp. 342-354.

10. Yanta, W.J.: *Use of the LDV in Subsonic and Supersonic Flow*. Proceedings of the Project Squid Workshop on the Use of the Laser Velocimeter for Flow Measurements, Purdue University, March 27-29, 1974, pp. 324-337.

11. Meyers, J.F.: *Applications of Laser Velocimetry to Large Scale and Specialized Aerodynamic Tests*. TSI Quarterly, Vol. V, Issue 4, pp. 5-12, November/December 1979.

12. Meyers, J.F.; Hunter, W.W., Jr.; Reubush, D.E.; Nichols, C.E.; Hepner, T.E.; and Lee, J.W.: *Performance Test of Laser Velocimeter System for the Langley 16-foot Transonic Tunnel*. NASA TP-2502, December 1985.

13. Hunter, W.W., Jr.; Gartrell, L.R.; Humphreys, W.M., Jr.; Witte, D.W.; and Nichols, C.E., Jr.: *Investigation and Development of a Laser Velocimeter for Langley's 20- inch Mach-6 Wind Tunnel*. Tenth National Aero-Space Plane Technology Symposium, paper 234, April 23-26, 1991.

14. Reyhner, T.A.: *Computation of Transonic Potential Flow About Three-Dimensional Inlets, Ducts, and Bodies*. NASA CR-3514, 1982.

15. Walsh, M.J.: *Influence of Particle Drag Coefficient on Particle Motion in High-Speed Flow With Typical Laser Velocimeter Applications*. NASA TN D-8120, 1976.

16. Nichols, C.E., Jr.: *Preparation of Polystyrene Microspheres for Laser Velocimetry in Wind Tunnels*. NASA TM-89163, June 1987.

17. Woods, M.E.; Dodge, J.S.; Krieger, I.M.; and Pierce, P.E.: *Emulsion Polymerization with Mixtures of Anionic and Nonionic Surfactants*. Paint Research Institute Proceedings, No. 61, Vol. 40, No. 527, December 1968, pp. 541-548.

18. Dodge, J.S.; Woods, M.E.; and Kreiger, I.M.: *Seed Polymerization Techniques Using Mixtures of Anionic and Nonionic Surfactants*. Paint Research Institute Proceedings, No. 70, Vol. 42, No. 541, February 1970, pp. 71-75.

19. Juang, M.S.: *Preparation of Monodisperse Polystyrene Latices by Emulsion Polymerization*. Ph. D. Thesis, Department of Chemistry, Case Western Reserve University, June 1975.

20. Mulholland, G.W.; Hartman, A.W.; Hembree, G.G.; Marx, E.; and Letieri, T.R.: *Development of a One-Micrometer-Diameter Particle Size Standard Reference Material*. Journal of Research of the National Bureau of Standards, Vol. 90, No. 1, January-February 1985, pp. 3-26.

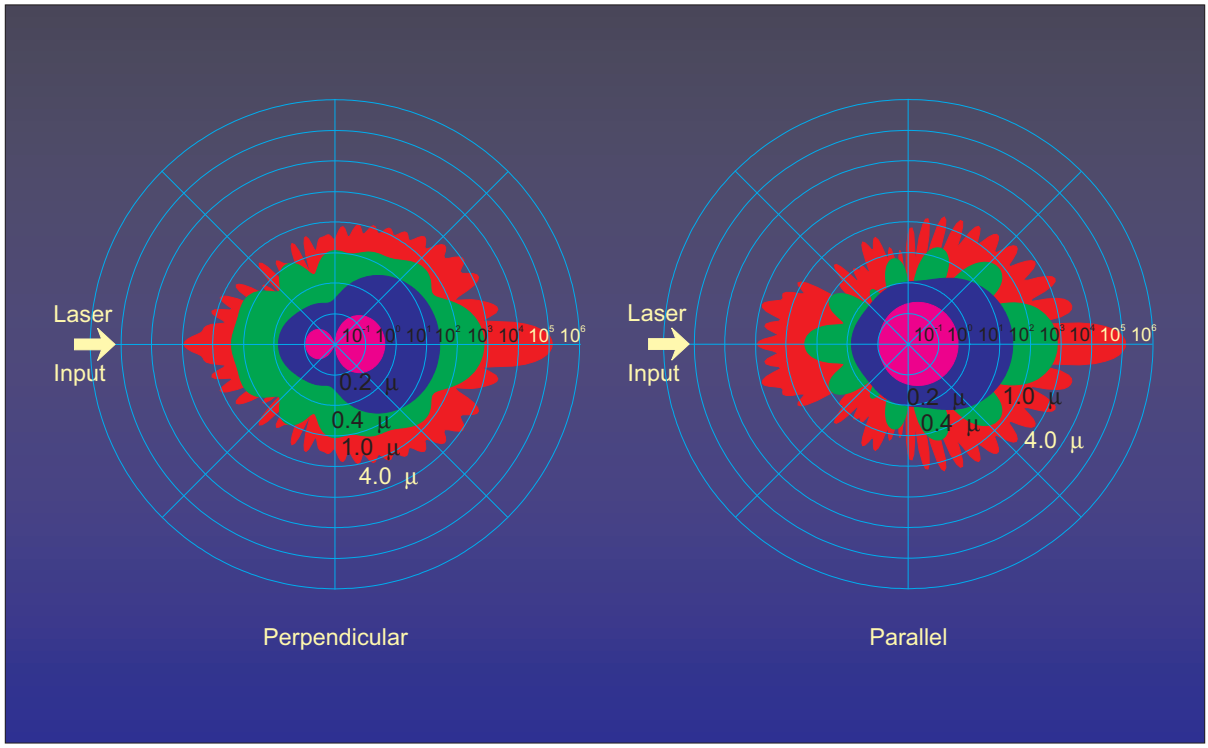

Figure 1.- Mie scattering, (Perpendicular and Parallel electric vectors) as a function of angle.

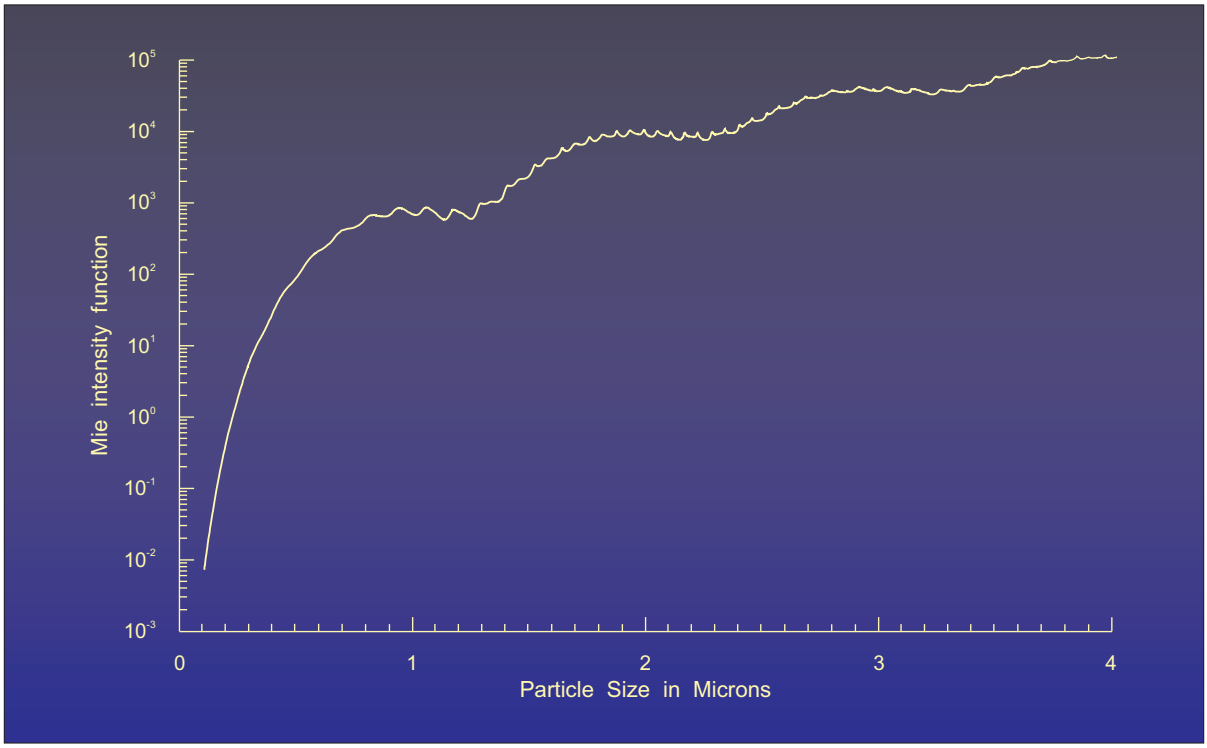

Figure 2.- Mie scattering as a function of particle size for a scattering angle of 2^{o}.

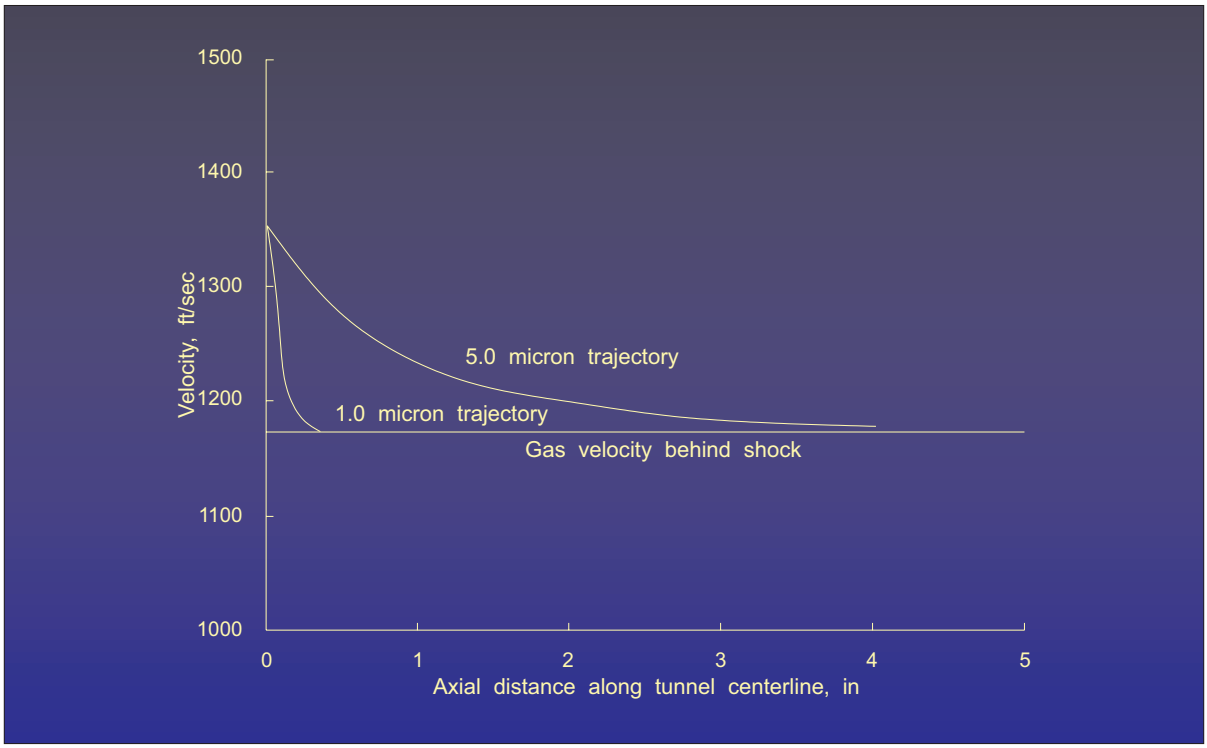

Figure 3.- Particle velocity relaxation behind an oblique shock located at 0, Mach number = 1.3.

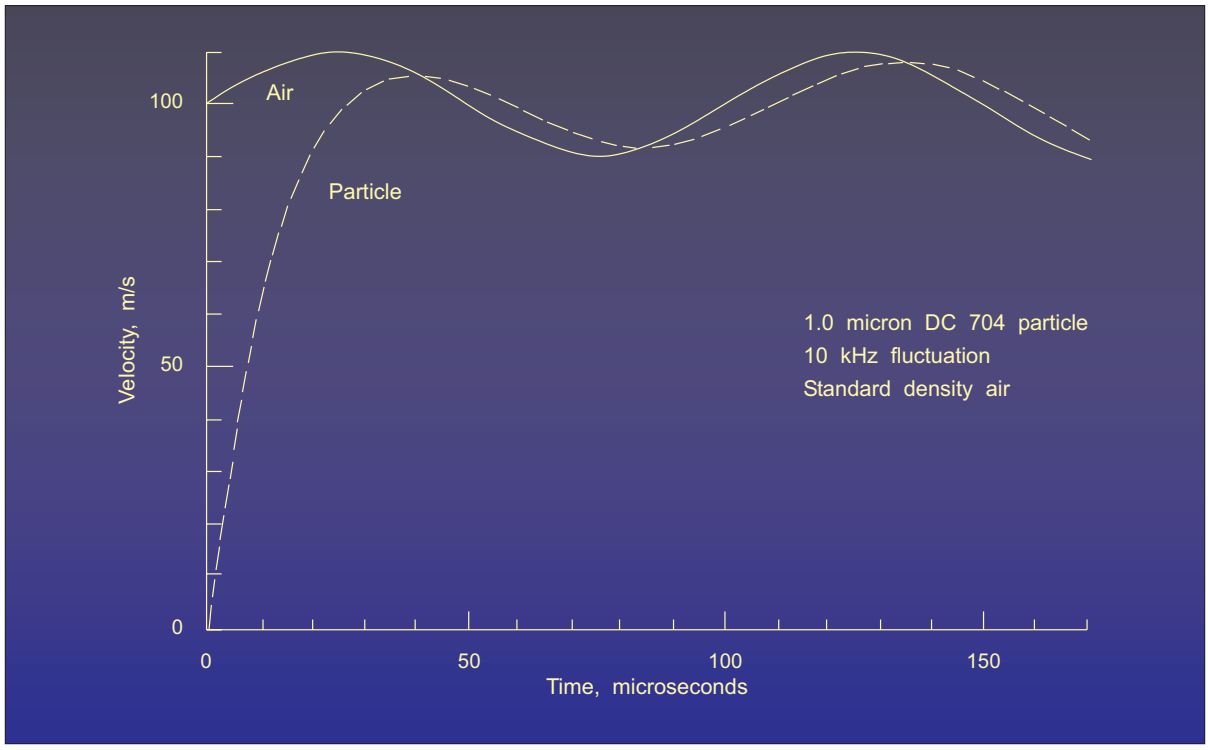

Figure 4.- Particle response to a fluctuating flow.

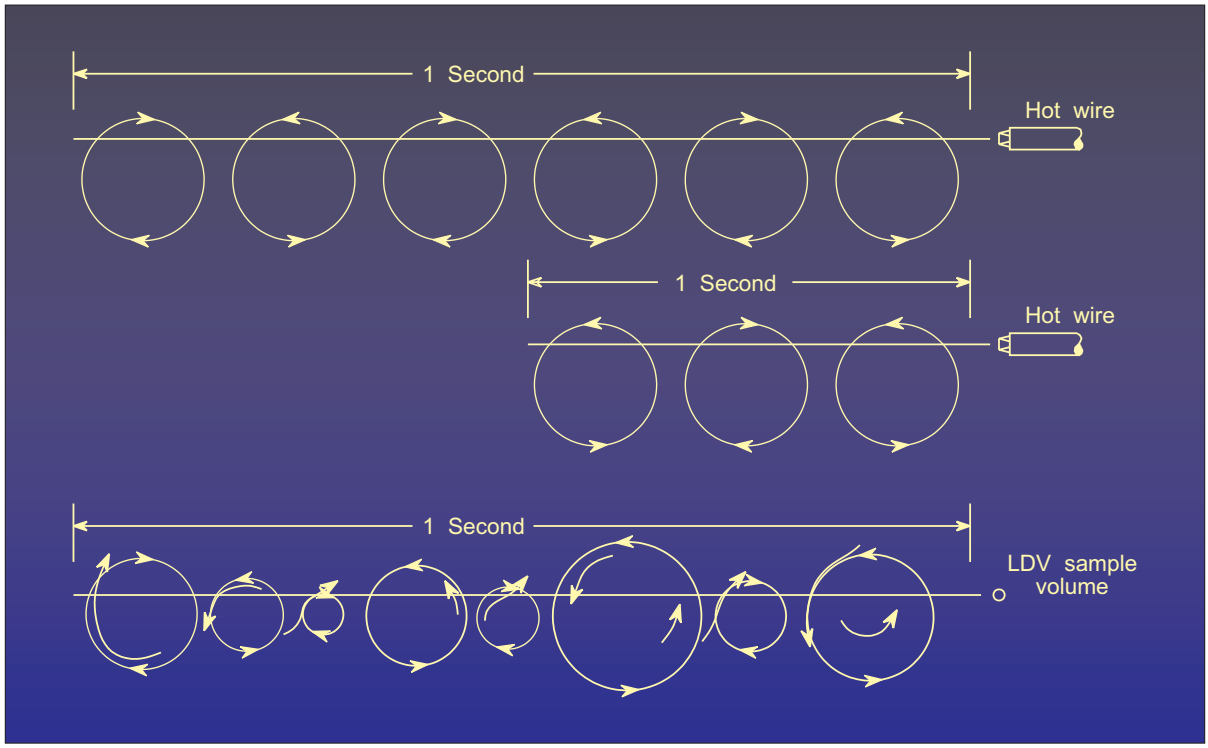

Figure 5.- Schematic of “frequency response.”

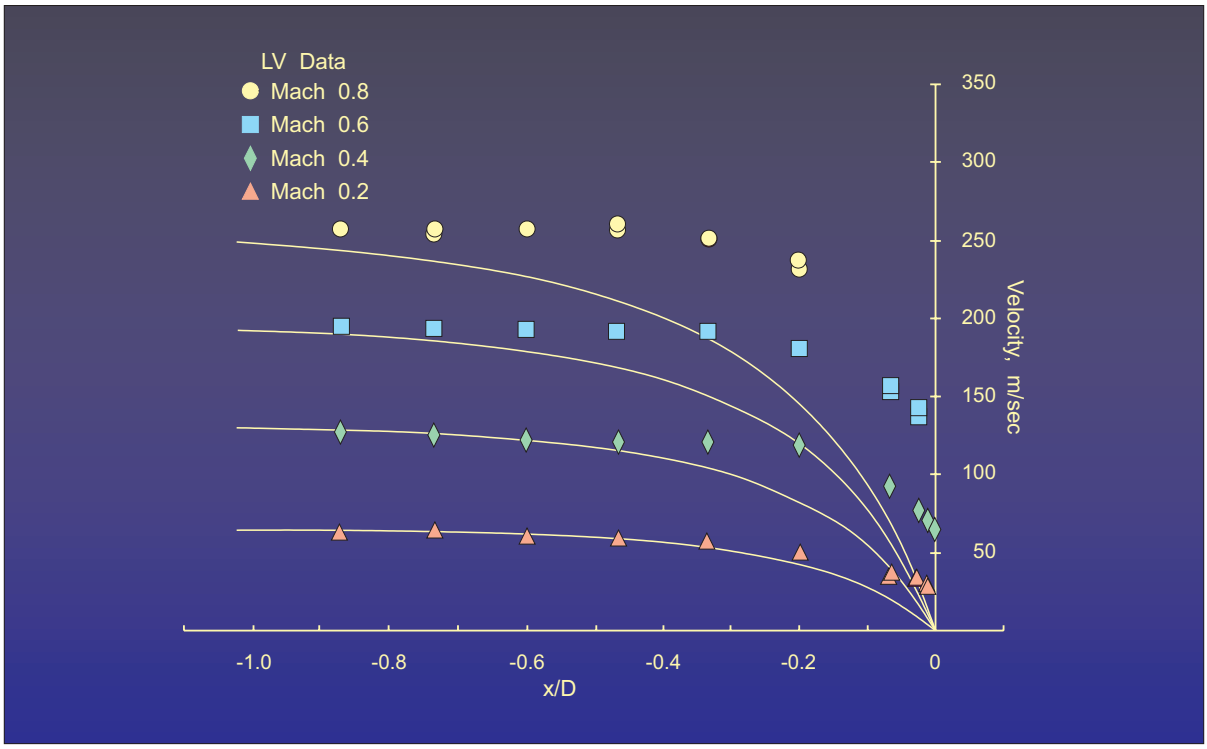

Figure 6.- Laser velocimeter measurements along the stagnating streamline of a hemisphere-cylinder model in the 16-foot transonic tunnel.

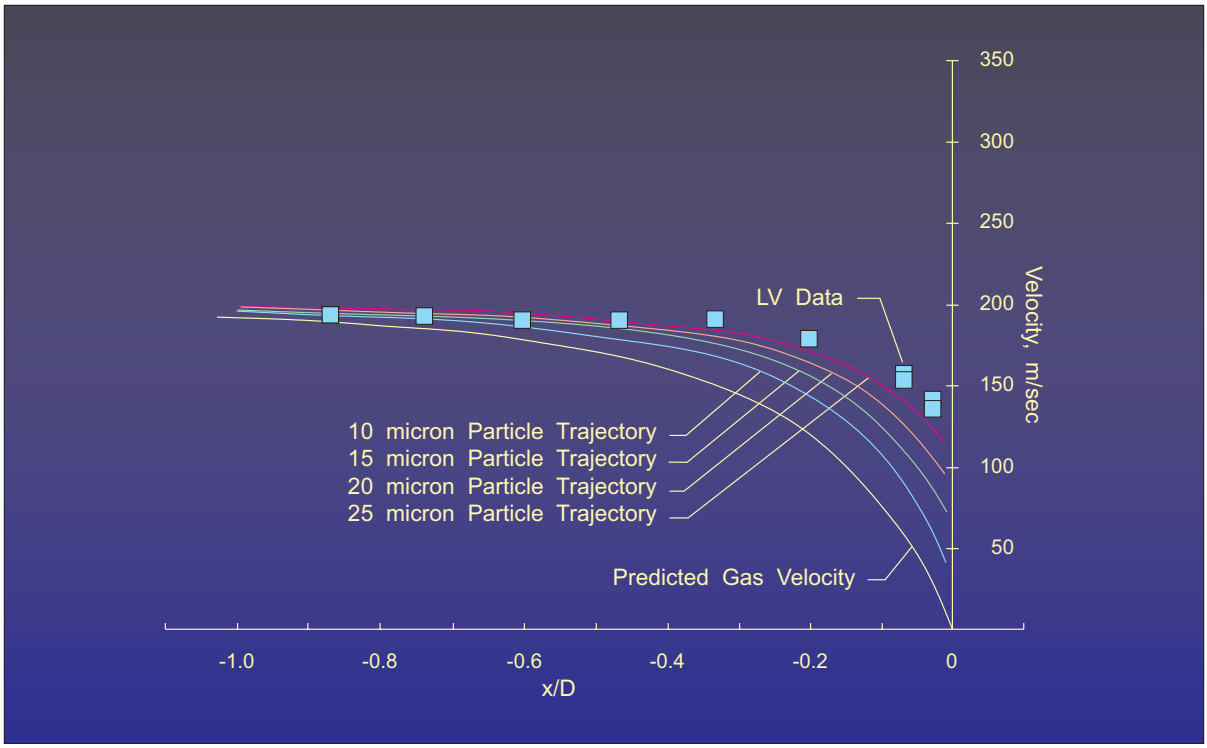

Figure 7.- Theoretical velocity profiles for various particle diameters along the stagnating streamline of a hemisphere-cylinder model in the 16-foot transonic tunnel.

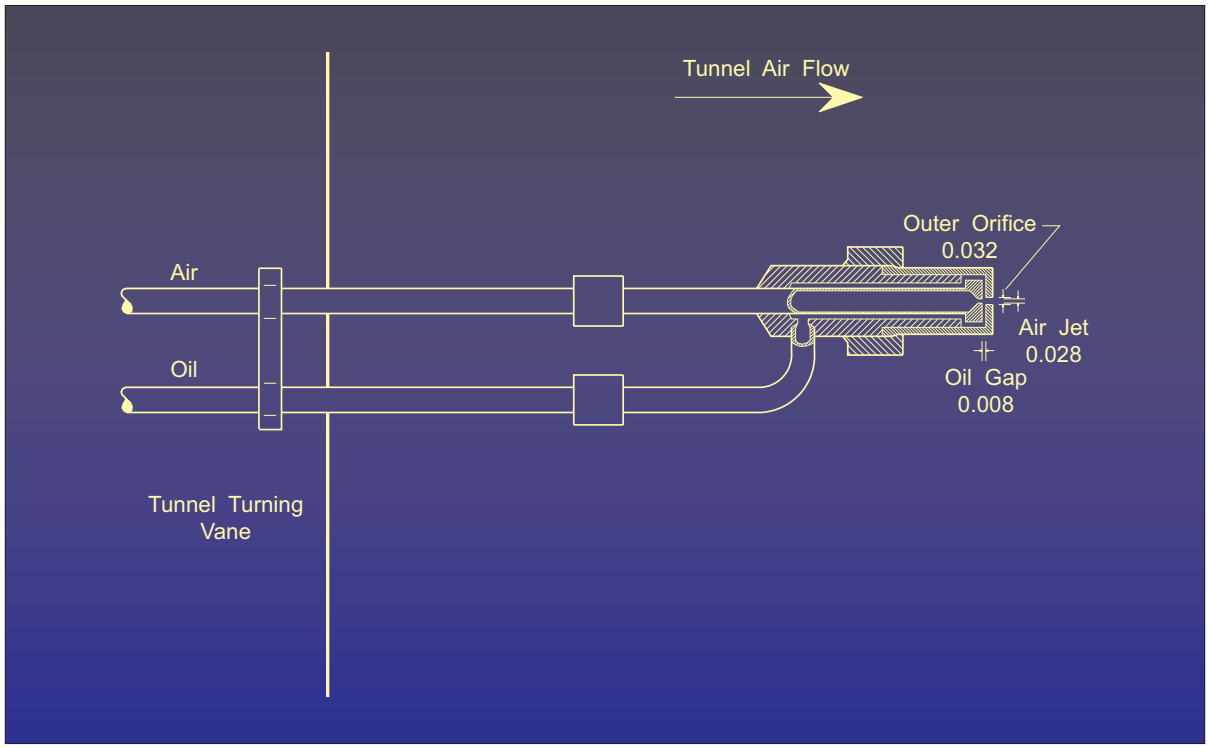

Figure 8.- Diagram of an oil/air atomization particle generator.

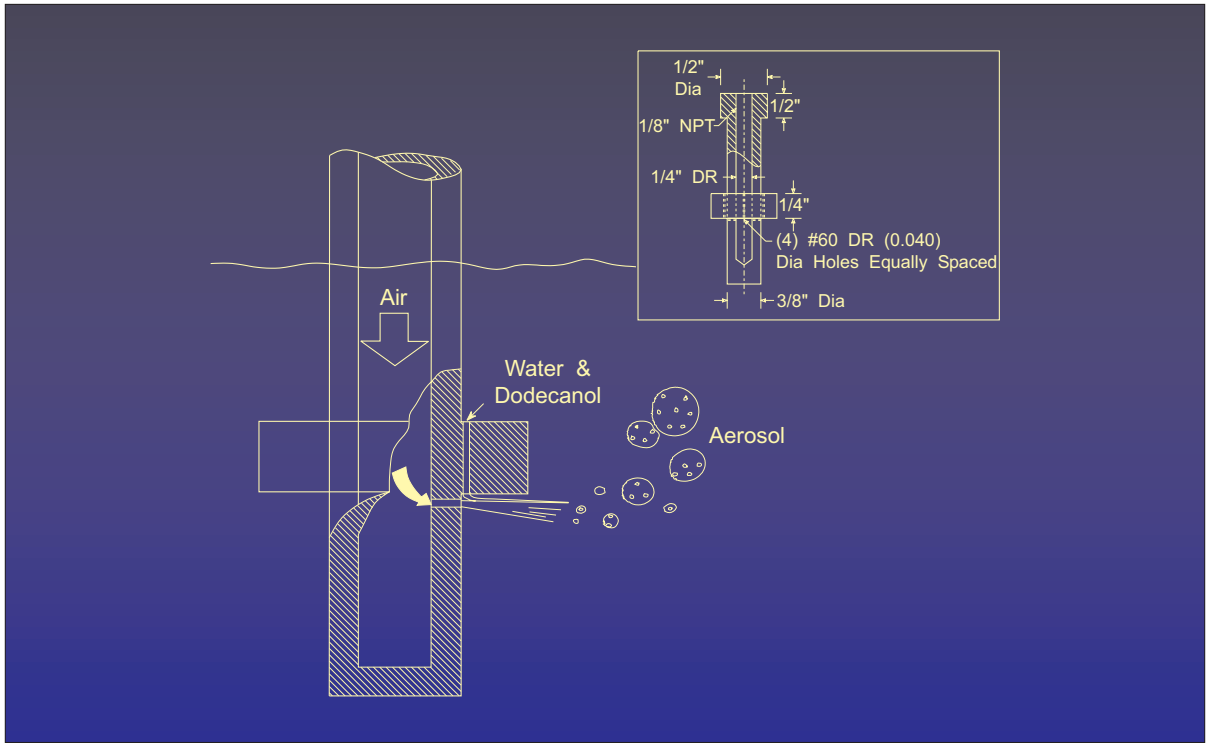

Figure 9.- Diagram of a Laskin nozzle.

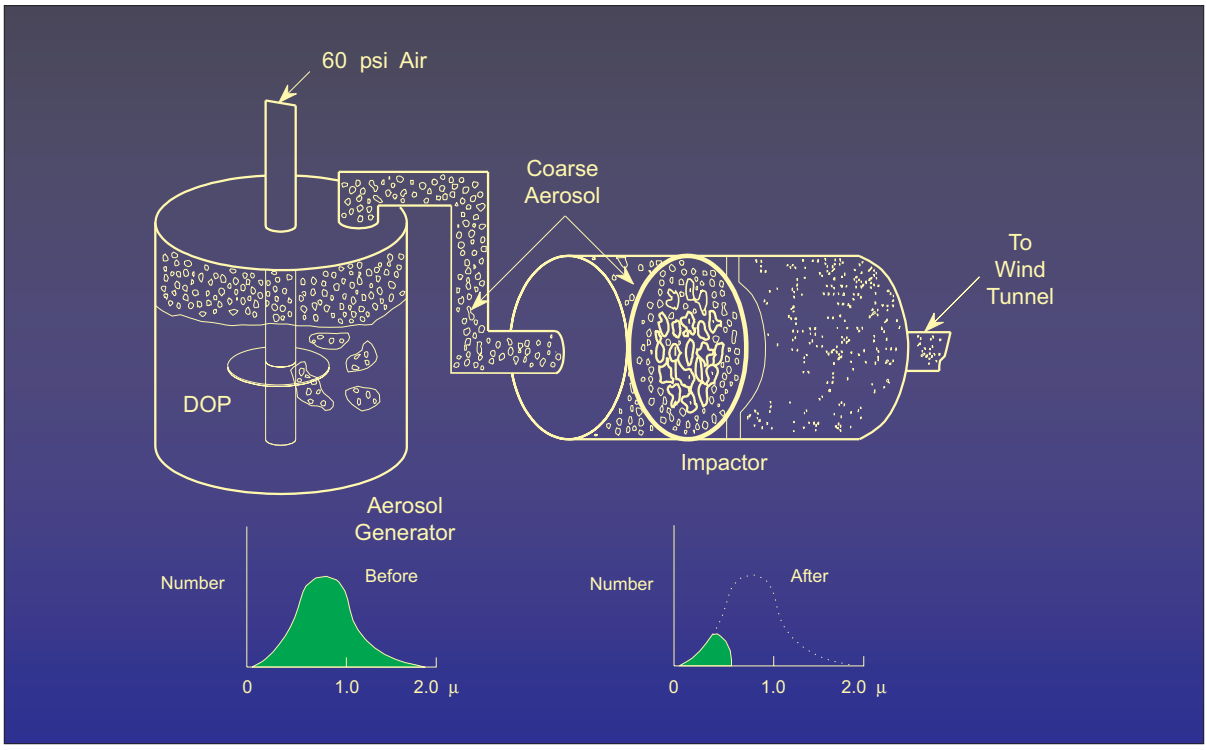

Figure 10.- Diagram of a Laskin nozzle with an impactor.

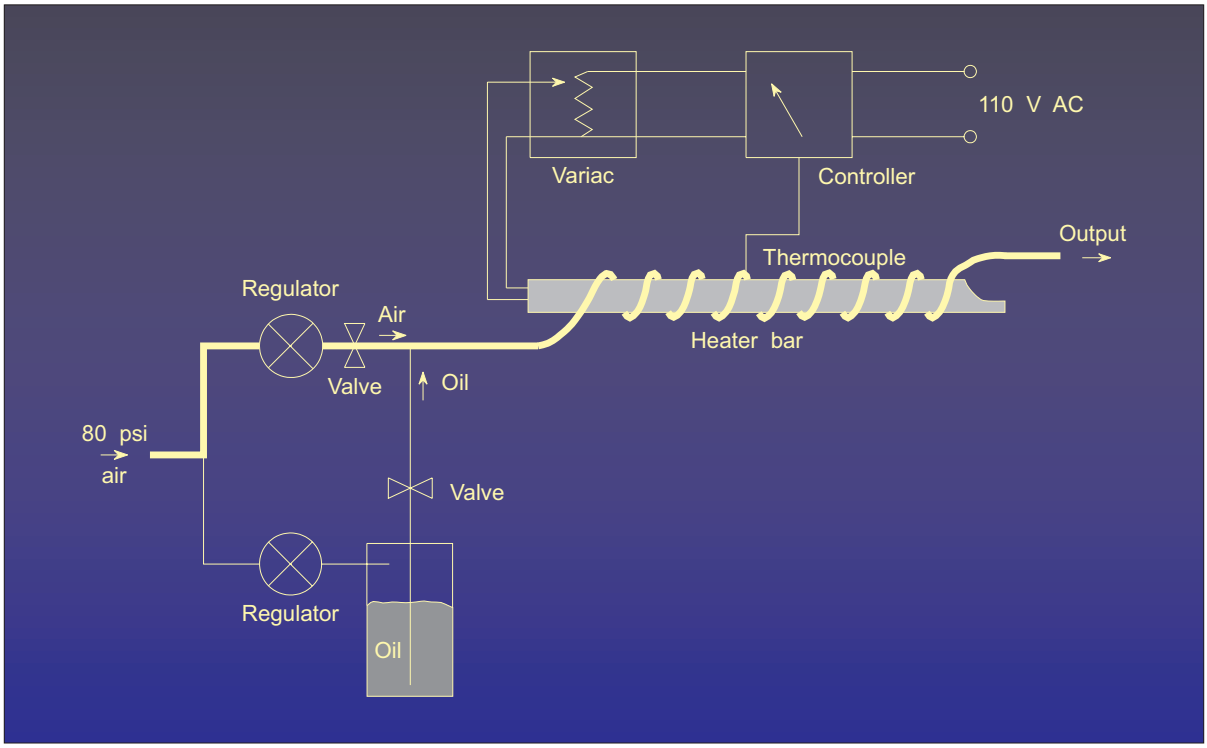

Figure 11.- Diagram of a vaporization / condensation generator.

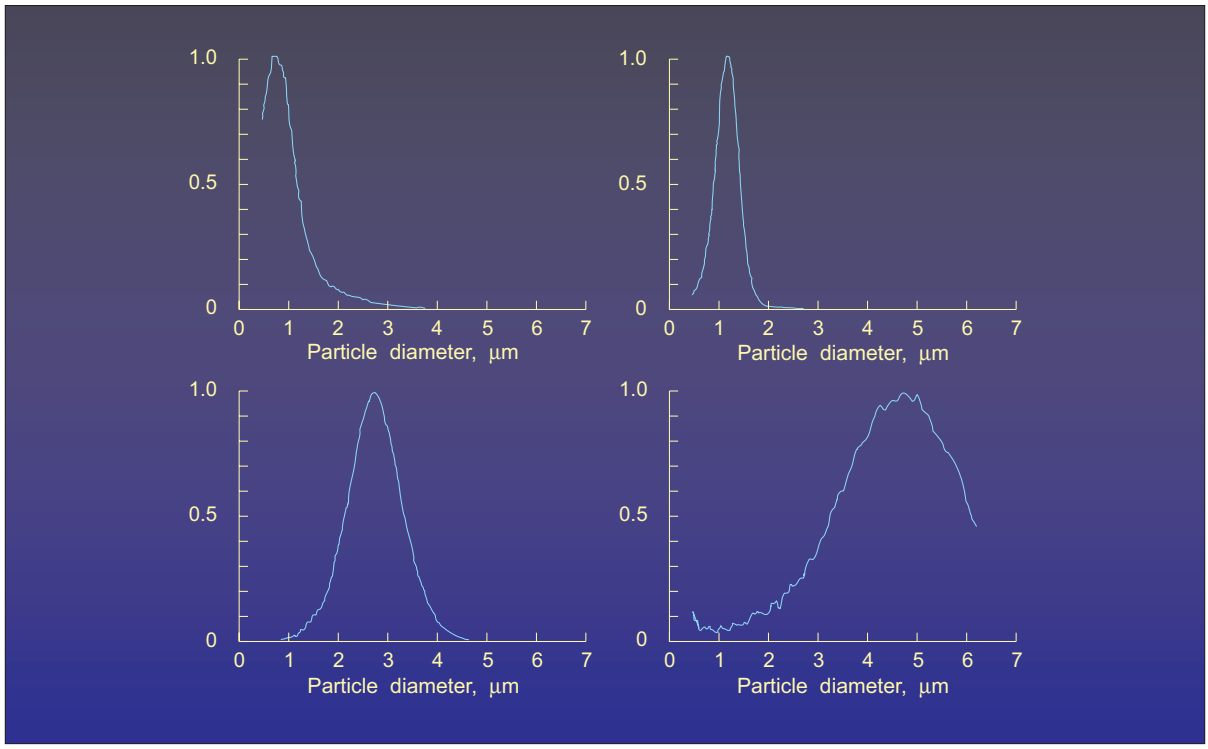

Figure 12.- Normalized particle size distribution for Dow Corning 704 diffusion pump oil from a vaporization/condensation generator at various exit velocities.

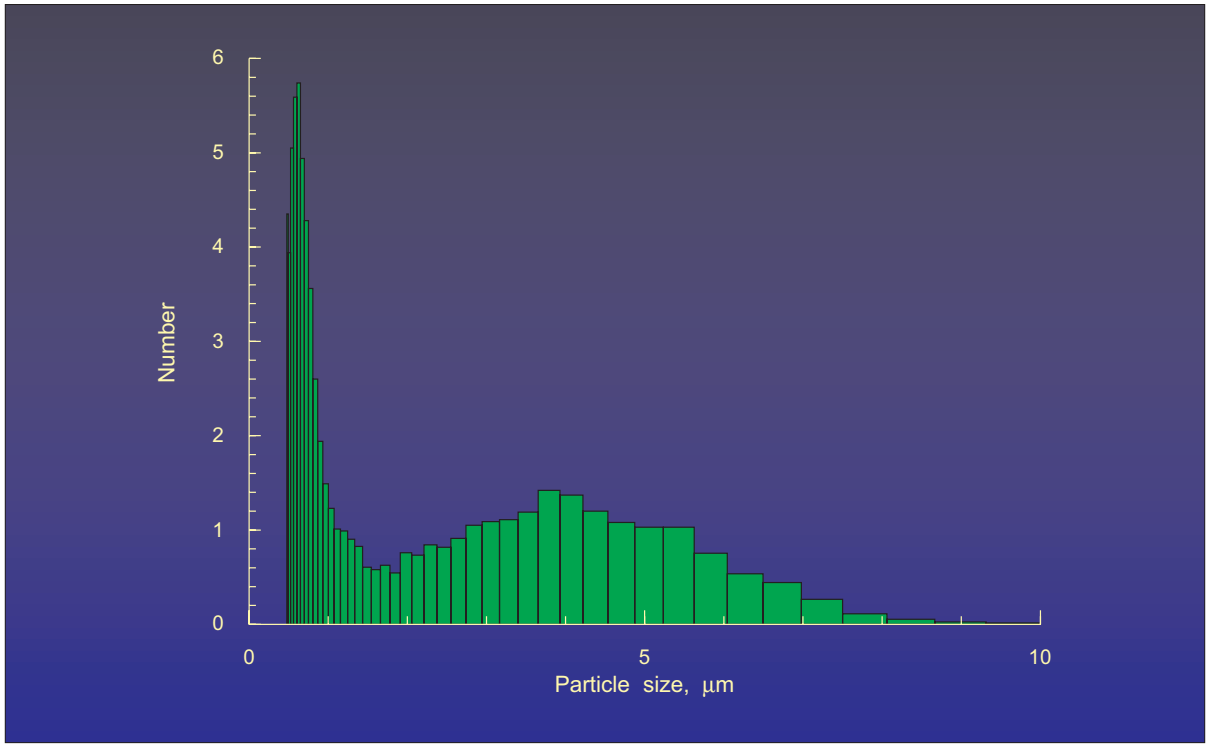

Figure 13.- Particle size distribution of propylene glycol from a vaporization/condensation generator, tunnel q = 0.0.

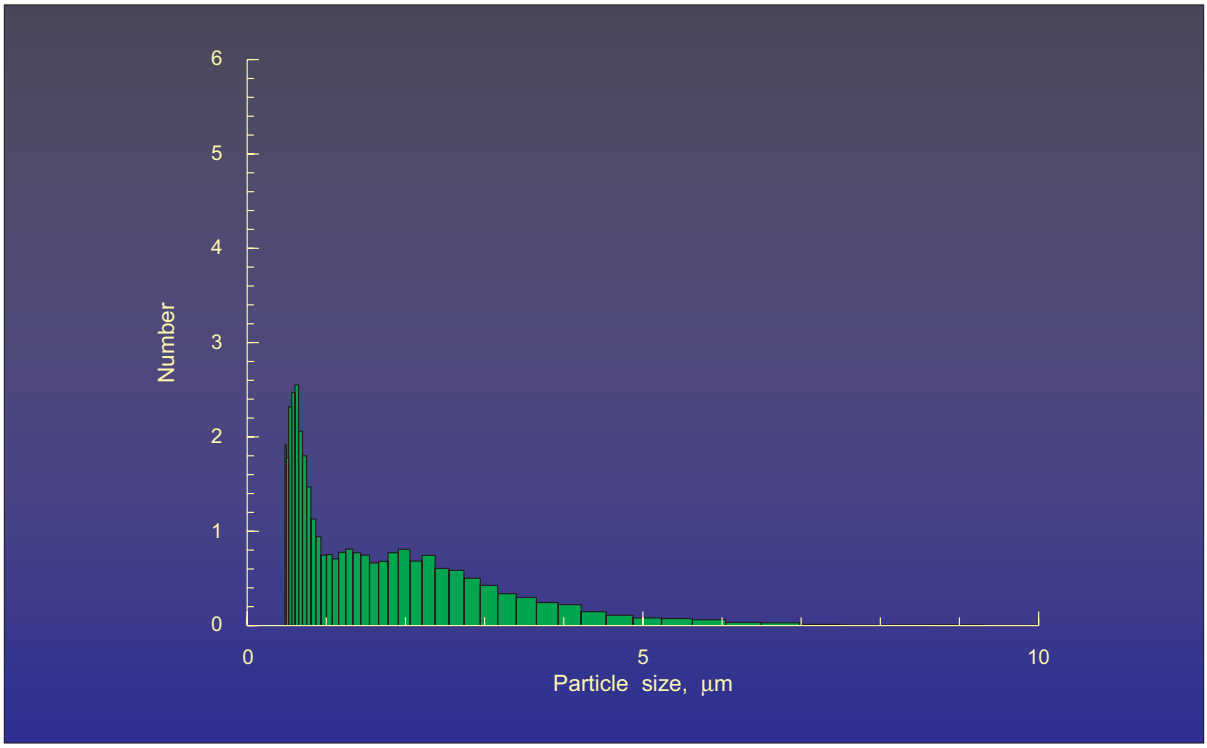

Figure 14.- Particle size distribution of propylene glycol from a vaporization/ condensation generator, tunnel q = 8.4.

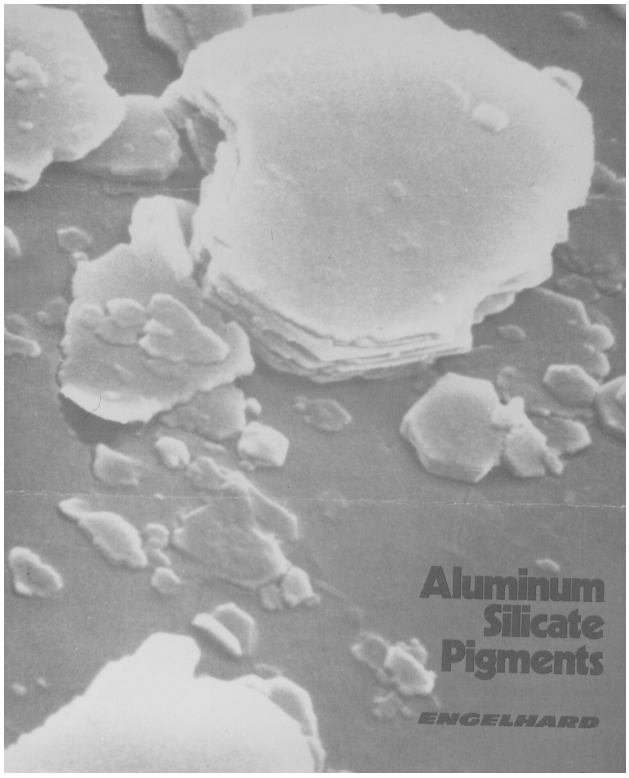

Figure 15.- Electron microscope photograph of aluminum silicate particles.

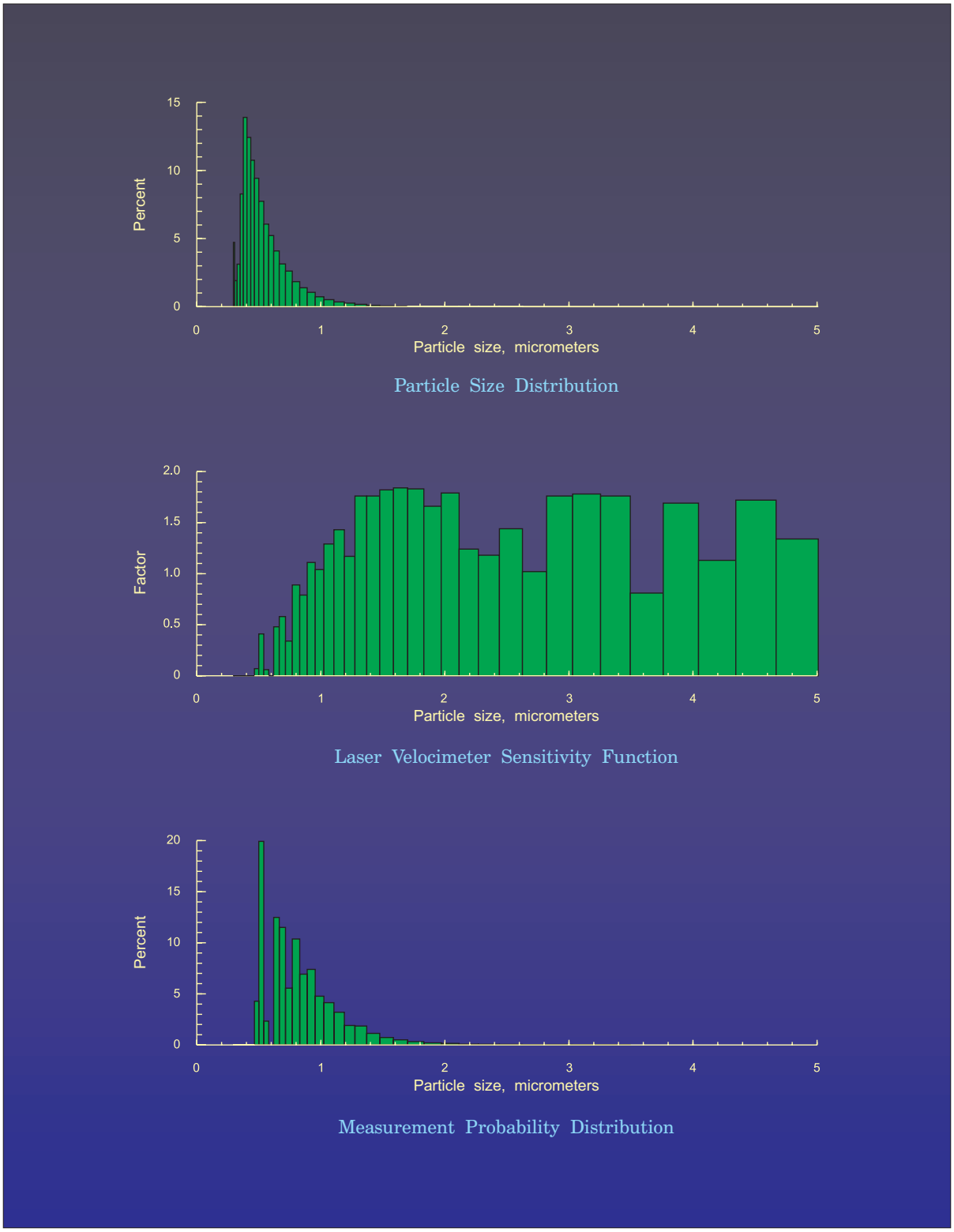

Figure 16.- Predicted laser velocimeter sensitivity function for aluminum silicate, 16-foot transonic tunnel.

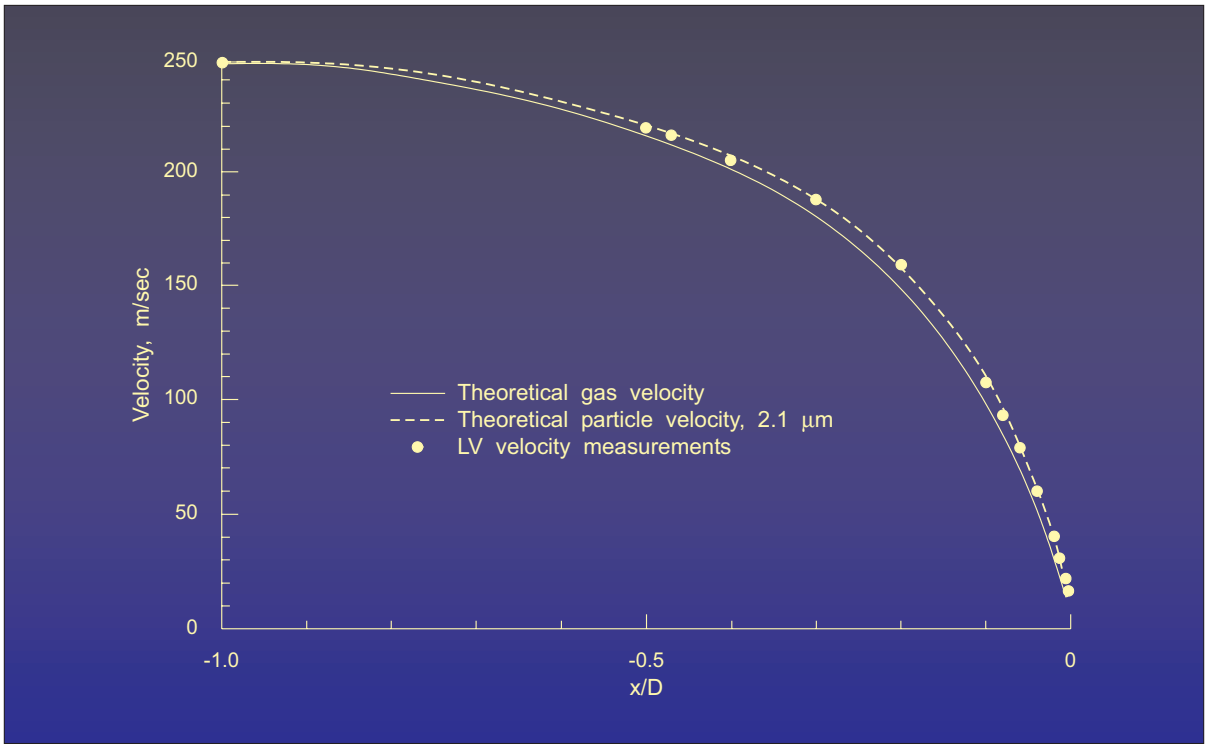

Figure 17.- U-component velocity along the stagnating streamline of a hemisphere-cylinder, Mach = 0.8.

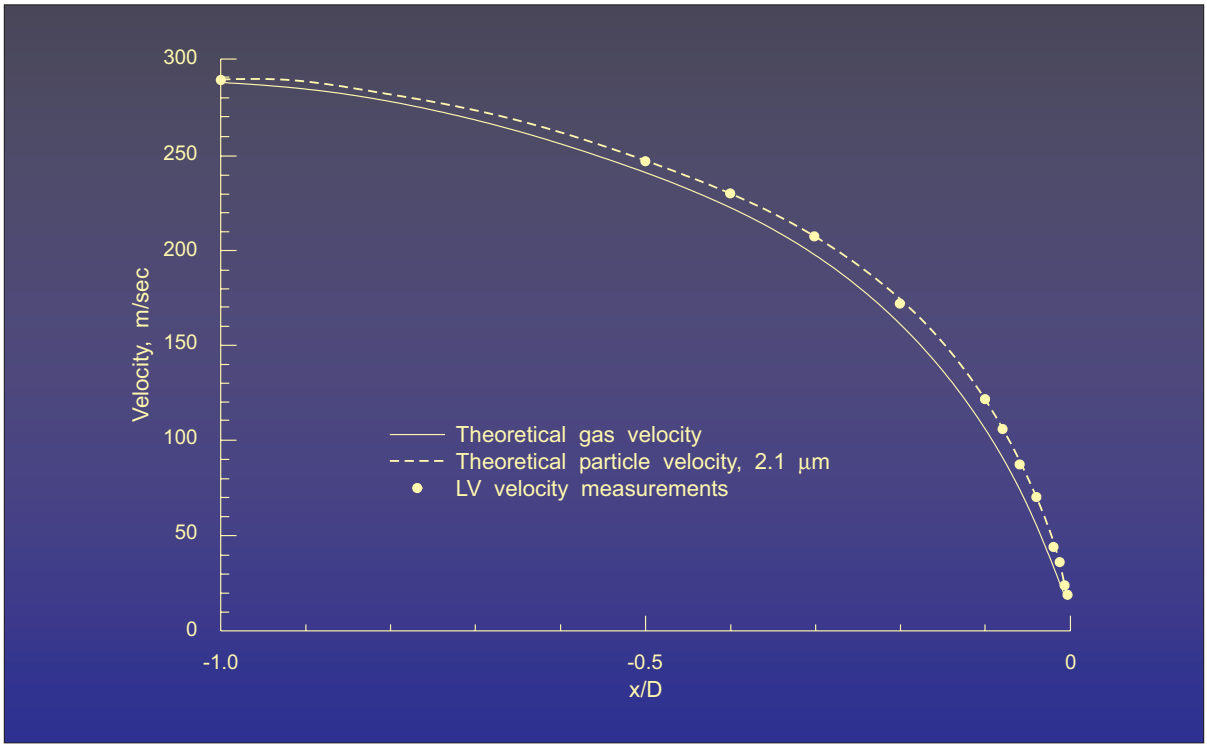

Figure 18.- U-component velocity along the stagnating streamline of a hemisphere-cylinder, Mach = 1.0.

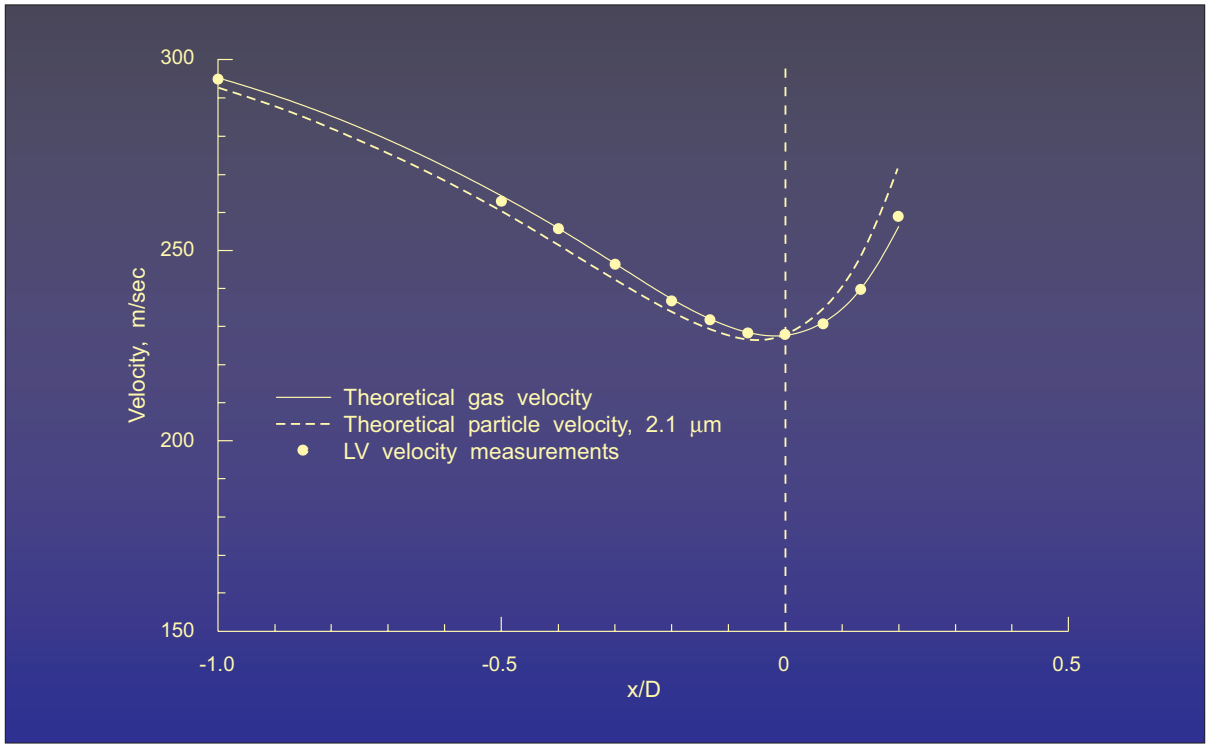

Figure 19.- U-component velocity along y/D = -0.533 of a hemisphere-cylinder, Mach = 1.0.

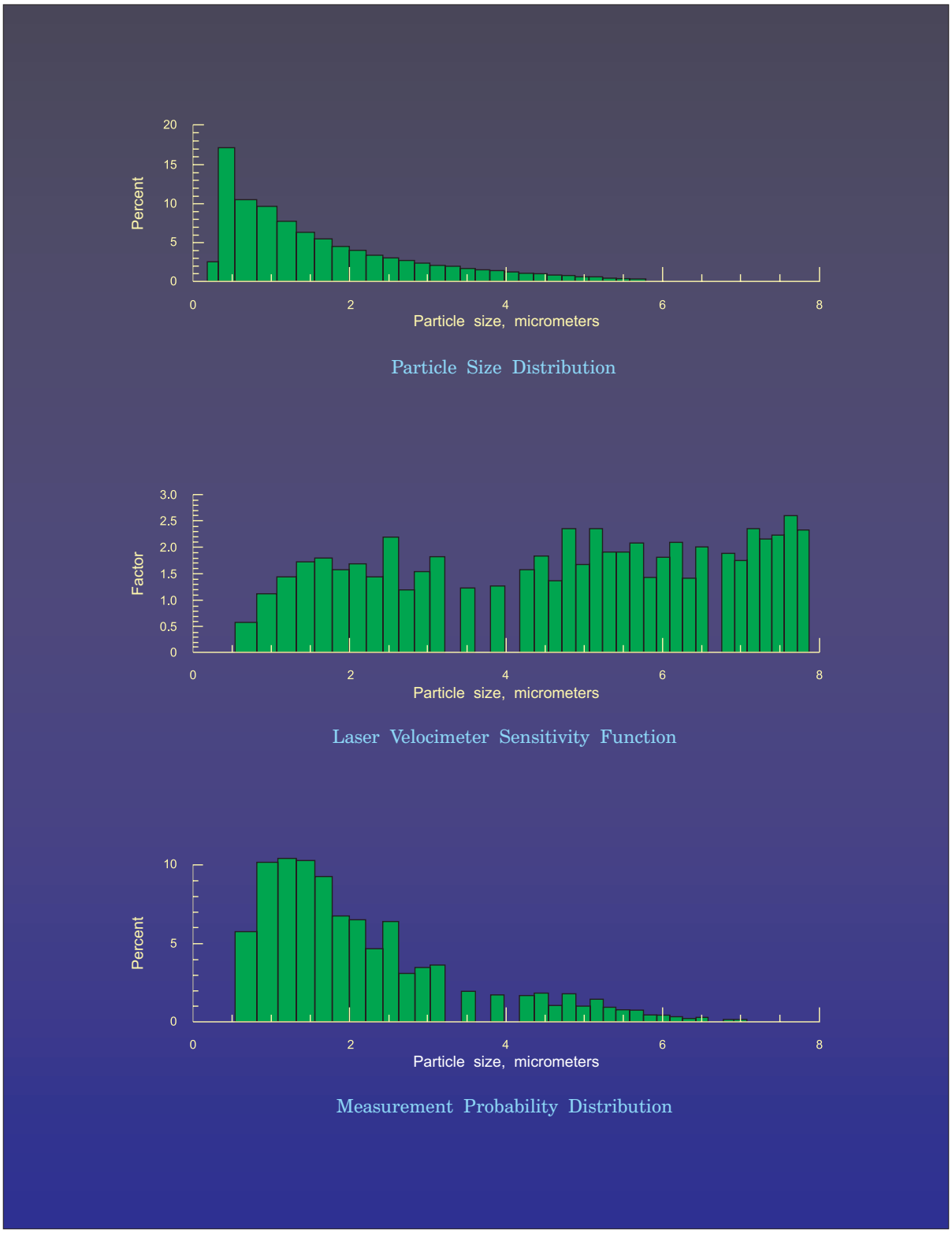

Figure 20.- Particle size distribution for aluminum silicate measured by an optical particle size analyzer.

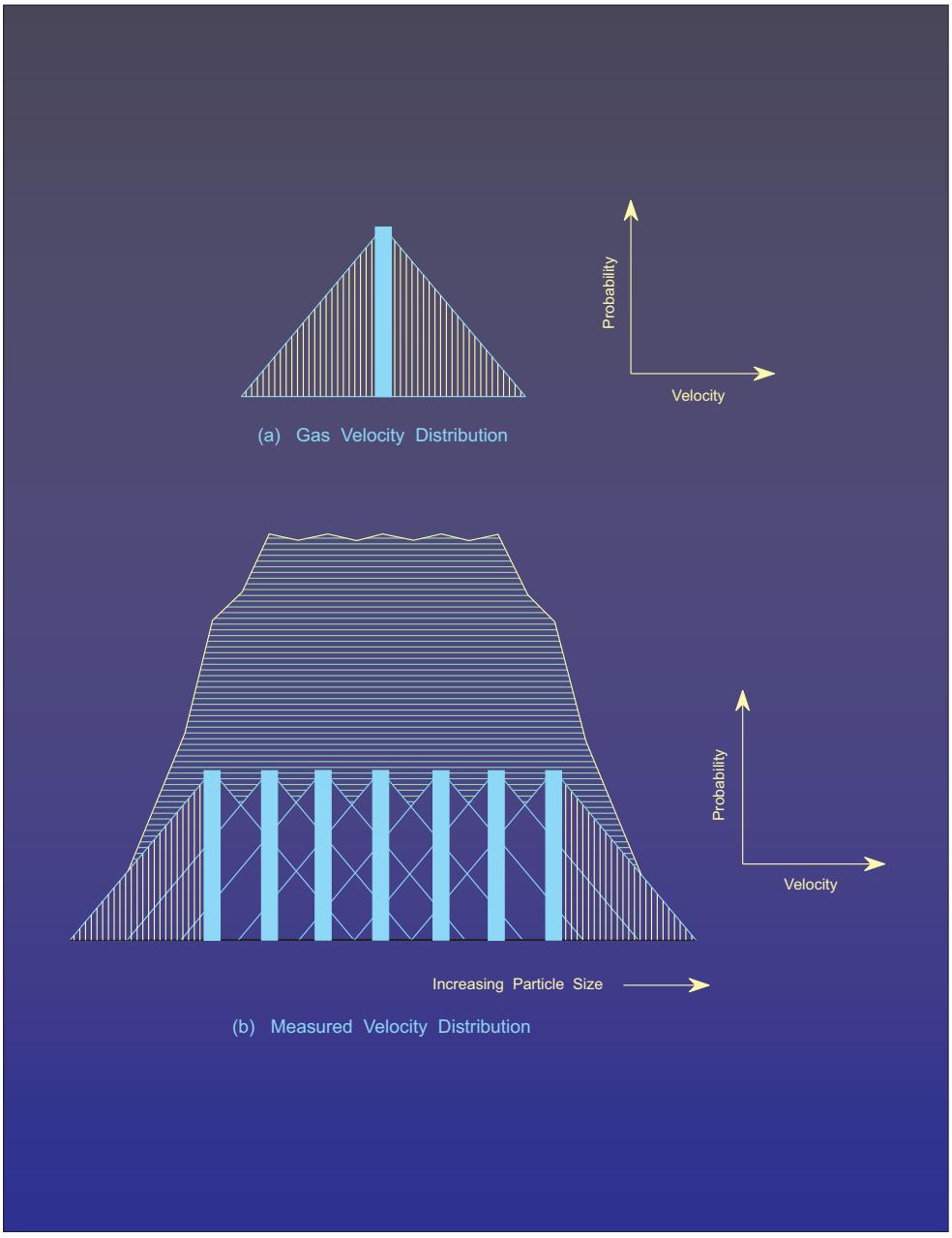

Figure 21.- Effect of particle size distribution on measured velocity.

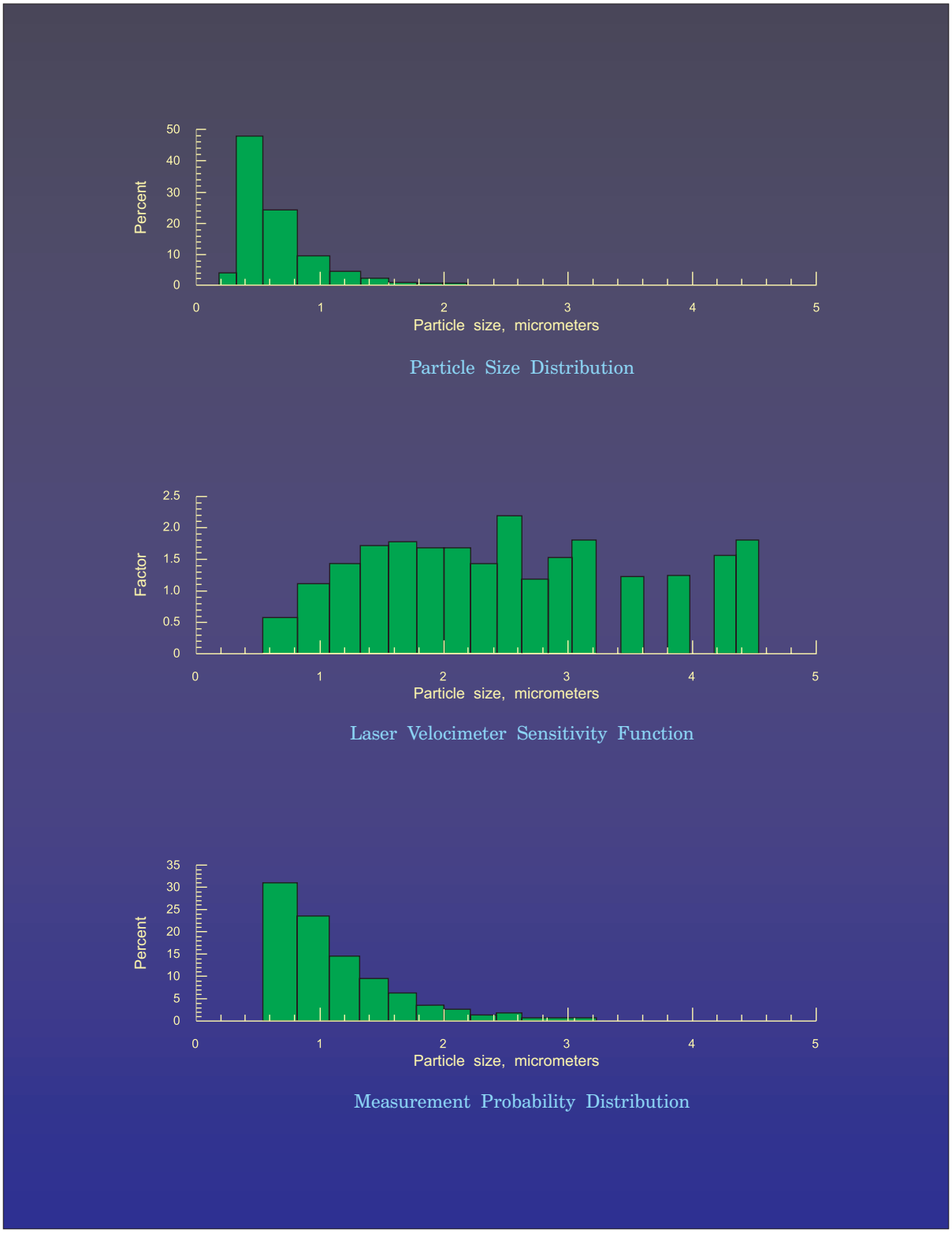

Figure 22.- Particle size distribution for aluminum silicate measured by an aerodynamic particle size analyzer.

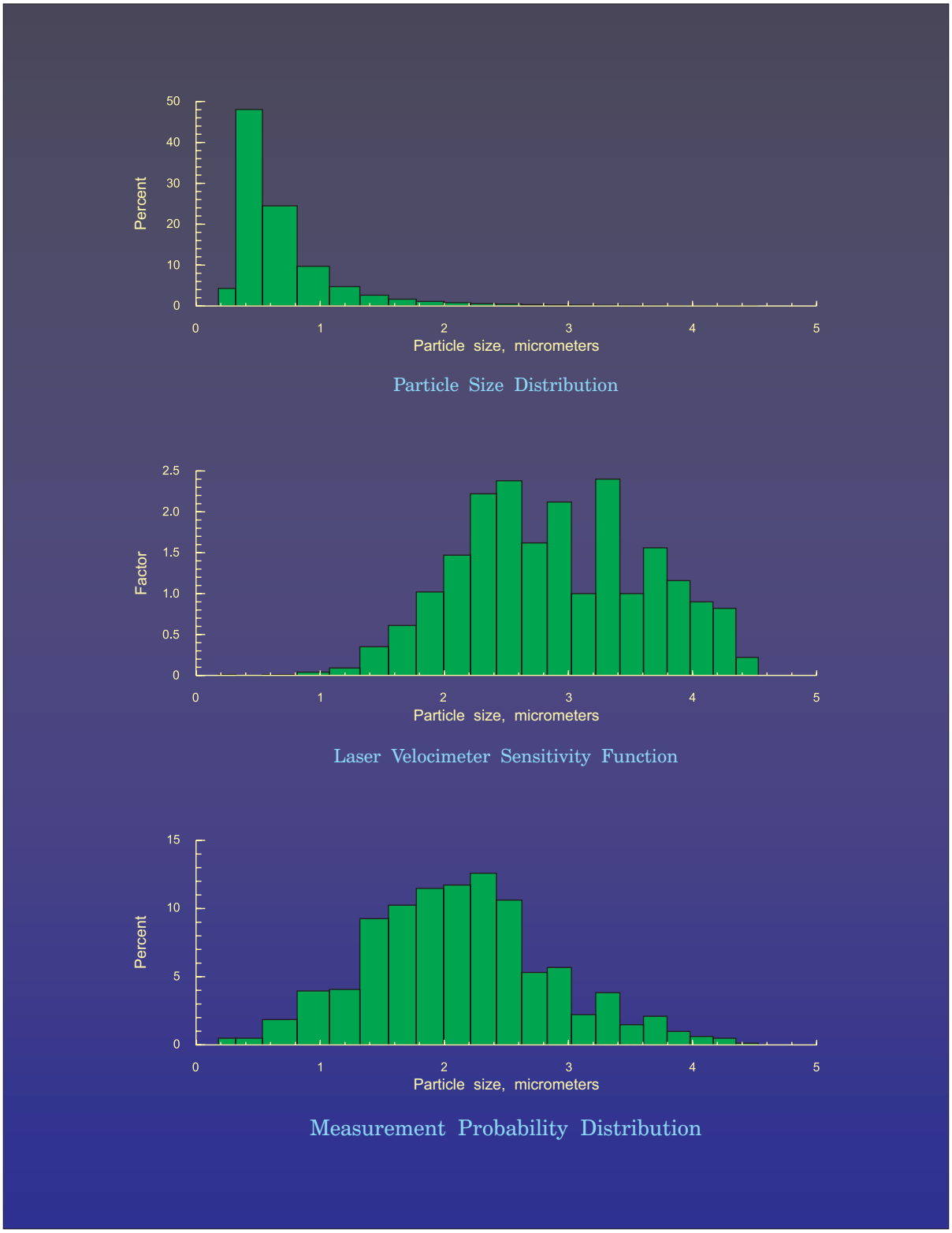

Figure 23.- Measured laser velocimeter sensitivity function based on the particle size distribution measured in the 16--foot transonic tunnel.

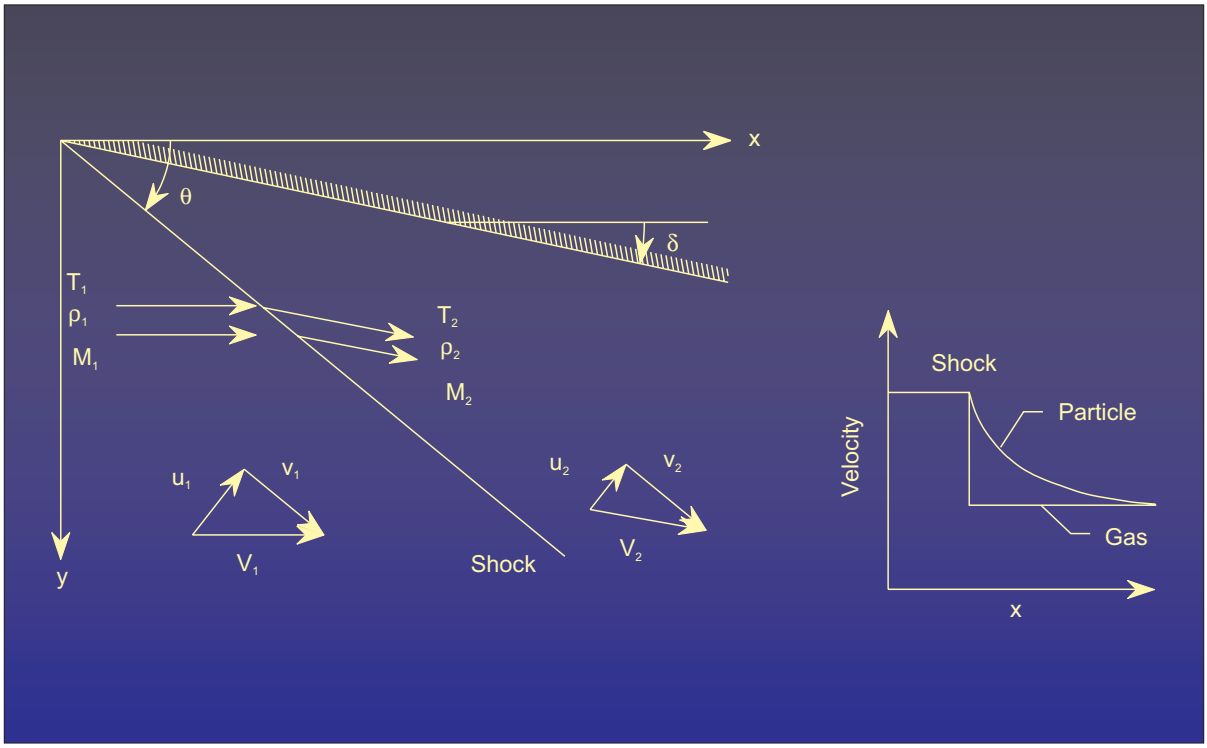

Figure 24.- Diagram of an oblique shock from a flat plate, Mach 6.

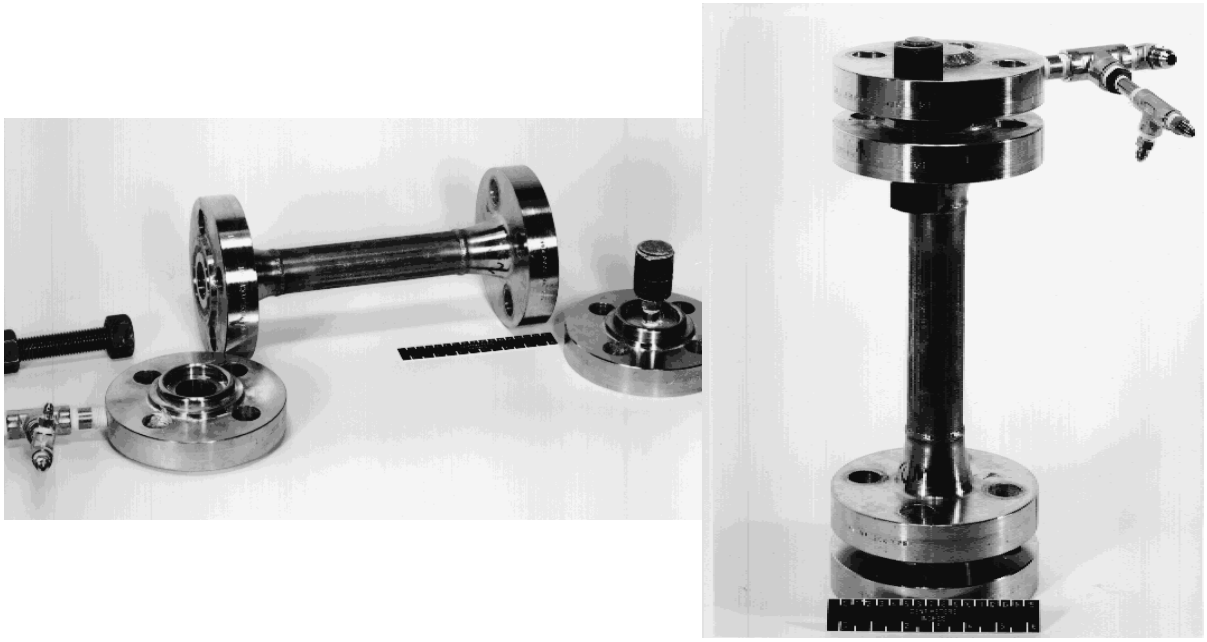

Figure 25.- Fluidized bed using 0.3 micron aluminum oxide particles for the 20-inch Mach 6 wind tunnel.

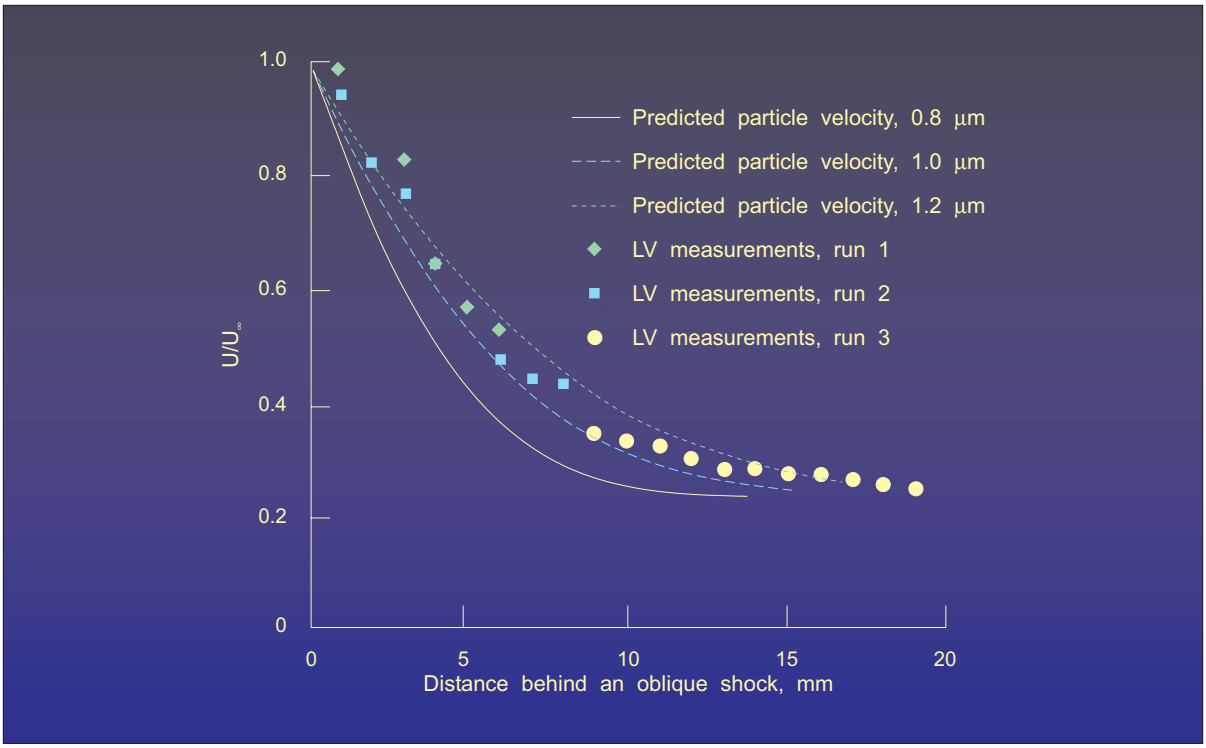

Figure 26.- Velocity downstream of an oblique shock at Mach 6 using 0.3 micron aluminum oxide particles.

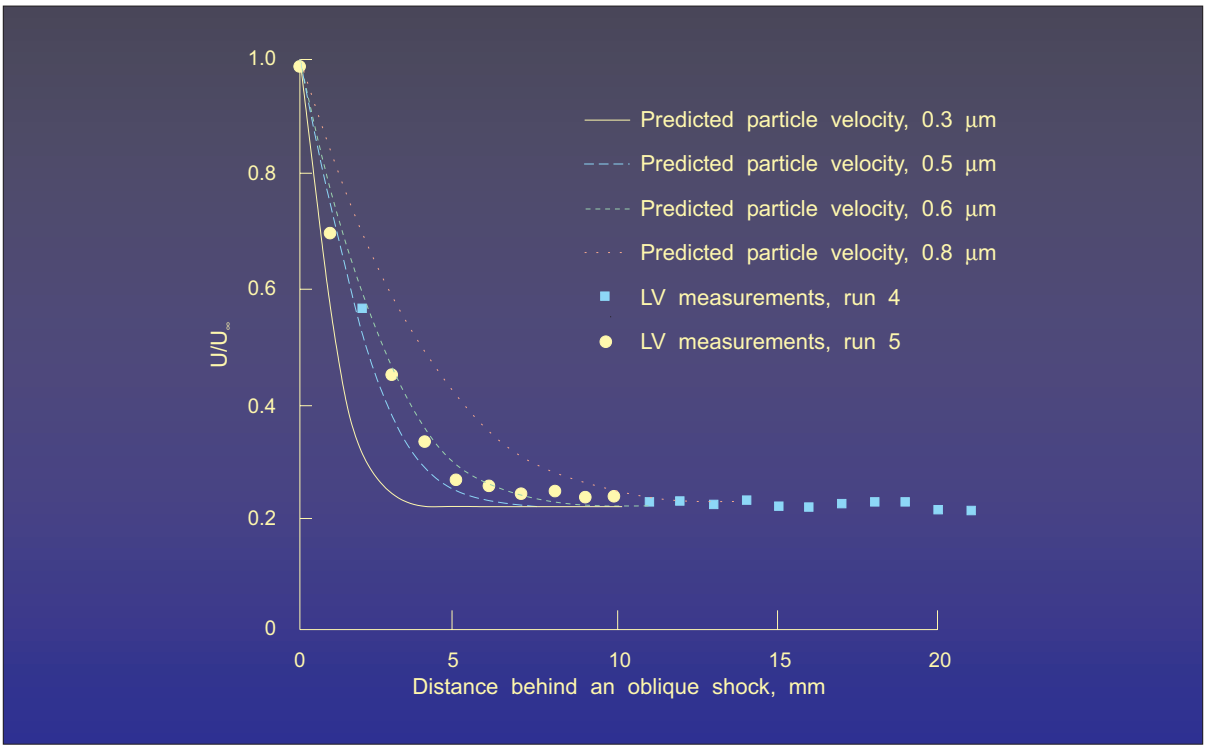

Figure 27.- Velocity downstream of an oblique shock at Mach 6 using “dry” 0.3 micron aluminum oxide particles.

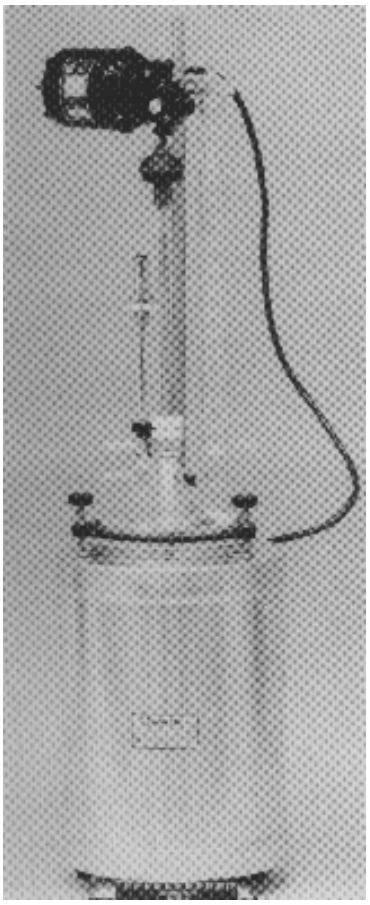

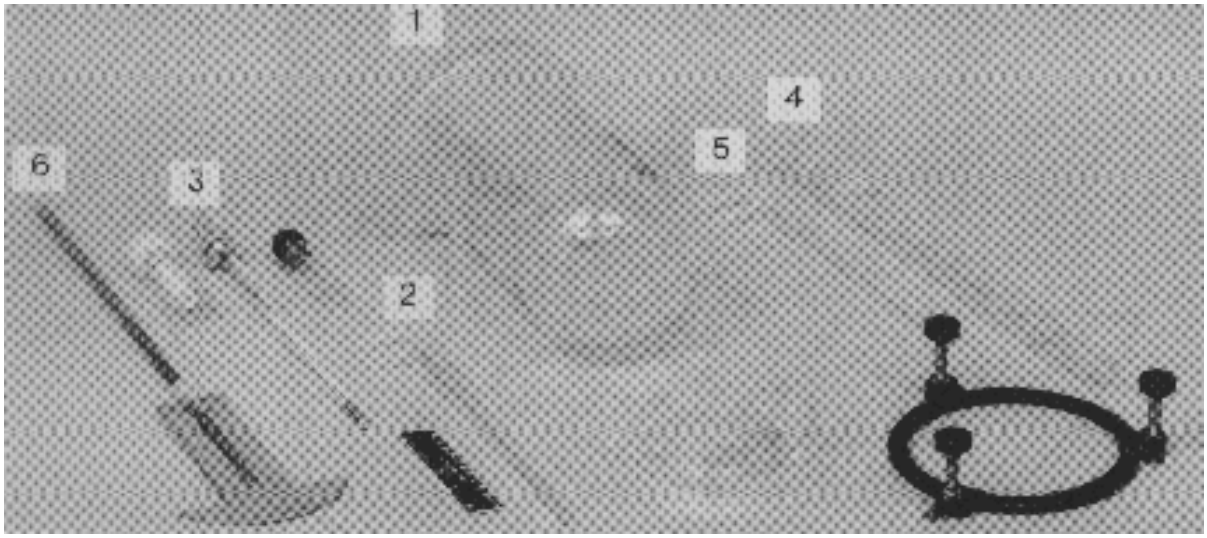

Figure 28.- Apparatus to make polystyrene microspheres.

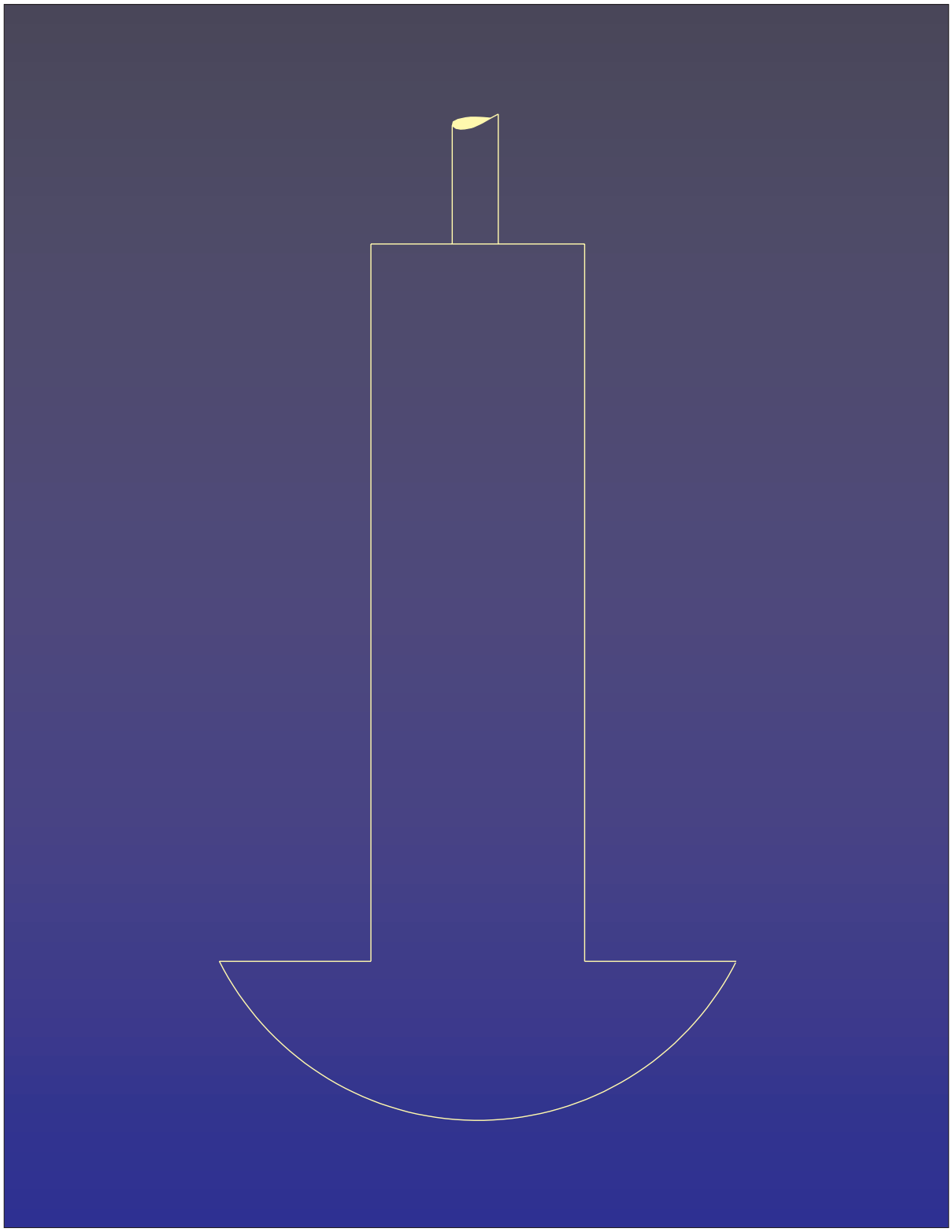

Figure 29.- Polystyrene stirring paddle.

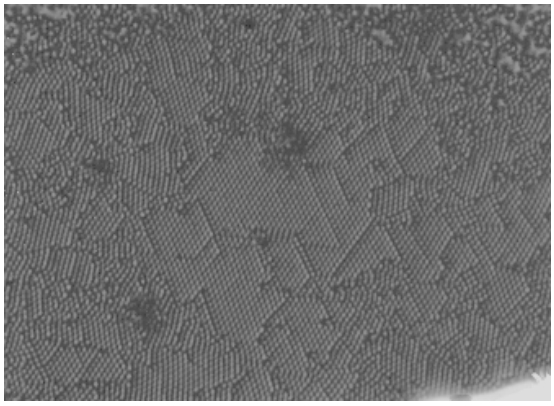

0.6 microns

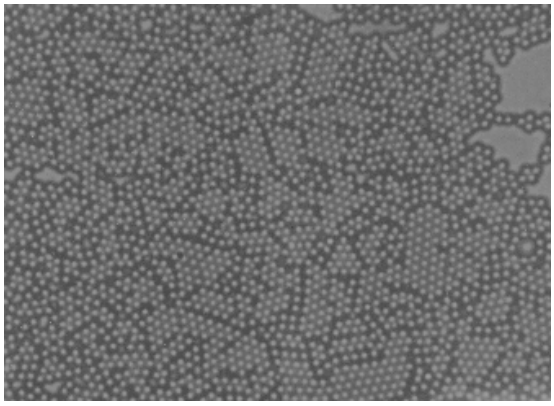

1.0 micron

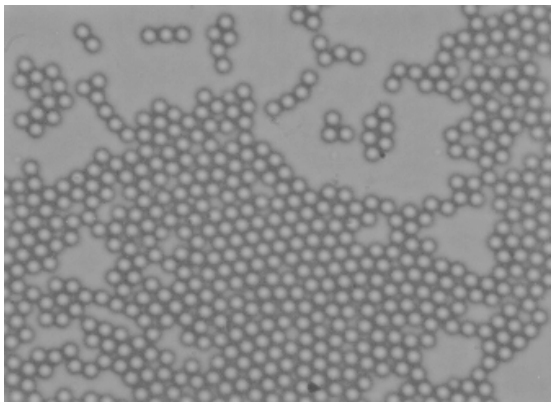

1.7 microns

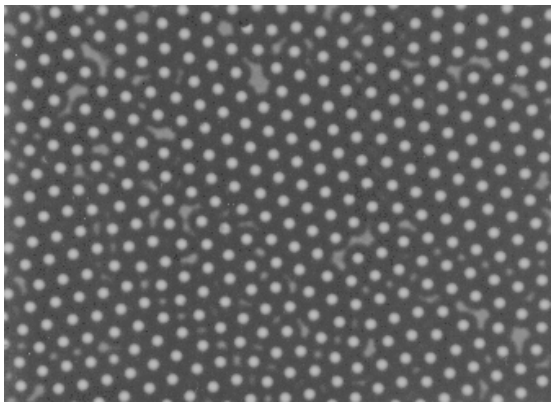

2.0 microns

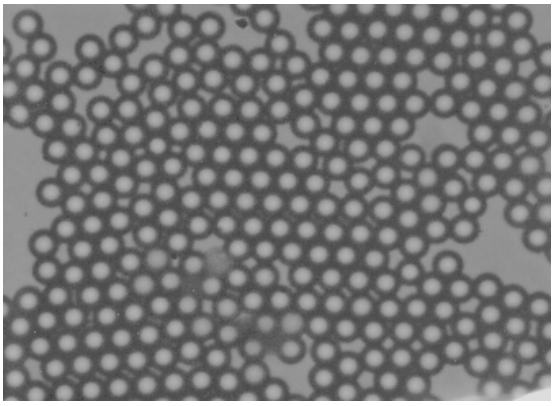

2.7 microns

Figure 30.- Microscope photographs of polystyrene microspheres, 2000x.

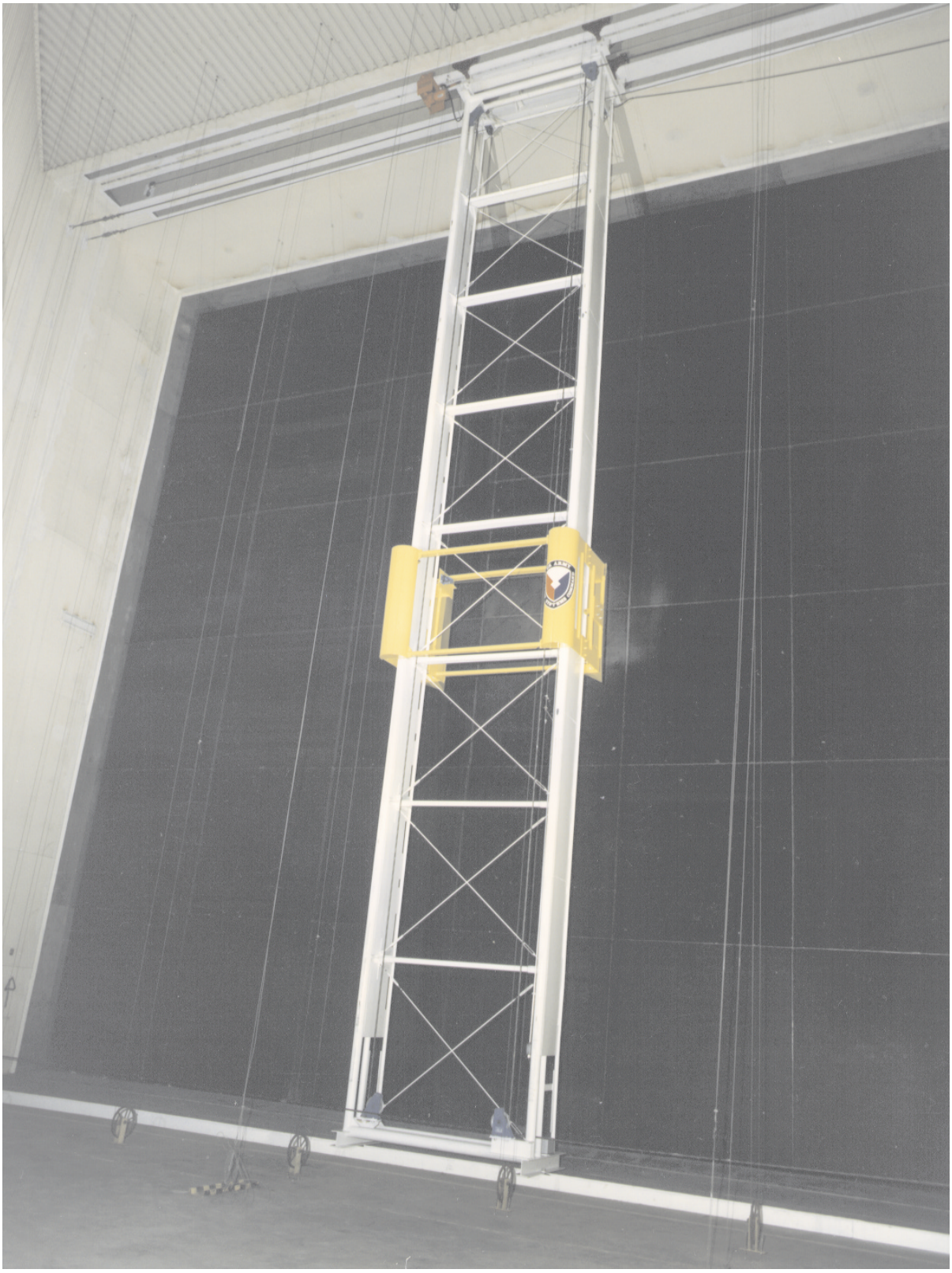

Figure 31.- Polystyrene particle generator system in the settling chamber of the 4x7- meter low speed wind tunnel.